



HAL
open science

A comparative study of image segmentation methods for micromechanical simulations of ductile damage

Victor-Manuel Trejo-Navas, Ante F Buljac, François Hild, Thilo F. Morgeneyer, Lukas Helfen, Marc Bernacki, Pierre-Olivier Bouchard

► To cite this version:

Victor-Manuel Trejo-Navas, Ante F Buljac, François Hild, Thilo F. Morgeneyer, Lukas Helfen, et al.. A comparative study of image segmentation methods for micromechanical simulations of ductile damage. Computational Materials Science, 2019, 159, pp.43-65. 10.1016/j.commatsci.2018.11.039 . hal-01950835

HAL Id: hal-01950835

<https://minesparis-psl.hal.science/hal-01950835v1>

Submitted on 11 Dec 2018

HAL is a multi-disciplinary open access archive for the deposit and dissemination of scientific research documents, whether they are published or not. The documents may come from teaching and research institutions in France or abroad, or from public or private research centers.

L'archive ouverte pluridisciplinaire **HAL**, est destinée au dépôt et à la diffusion de documents scientifiques de niveau recherche, publiés ou non, émanant des établissements d'enseignement et de recherche français ou étrangers, des laboratoires publics ou privés.

A comparative study of image segmentation methods for micromechanical simulations of ductile damage

Victor Manuel Trejo Navas¹ Ante Buljac^{2,3}
François Hild² Thilo Morgeneyer³ Lukas Helfen^{4,5}
Marc Bernacki¹
Pierre-Olivier Bouchard¹

¹MINES ParisTech, PSL Research University,
CEMEF-Centre de mise en forme des matériaux, CNRS UMR 7635,
CS 10207 rue Claude Daunesse, 06904 Sophia Antipolis Cedex, France

²Laboratoire de Mécanique et Technologie (LMT),
ENS Paris-Saclay, CNRS, Université Paris-Saclay,
61 avenue du Président Wilson, 94235 Cachan Cedex, France

³MINES ParisTech, PSL Research University,
Centre des Matériaux, CNRS UMR 7633, BP 87, 91003 Evry, France

⁴Institute for Proton Science and Synchrotron Radiation,
Karlsruhe Institute of Technology (KIT),
76131 Karlsruhe, Germany

⁵European Synchrotron Radiation Facility (ESRF),
38043 Grenoble, France

Abstract

The influence of image segmentation on micromechanical simulations of ductile damage in nodular graphite cast iron coupled with 3D imaging is explored for two tensile specimens. Three different approaches are used to segment the microstructures from laminography data. These microstructures are immersed in a finite element mesh and simulations with experimental boundary conditions are carried out for each of the three segmentation techniques. The sensitivity of local and global mechanical quantities is assessed based on the results of these simulations. The comparison between the employed techniques is then used to estimate the uncertainty associated with the image segmentation stage.

1 Introduction

Micromechanical simulations based on three-dimensional imaging techniques are becoming popular to study the behavior of heterogeneous microstructures [1, 2, 3, 4, 5]. In the context of ductile damage, this route enhances the possibilities for studying the corresponding micromechanisms (*i.e.*, void nucleation, growth, and coalescence). With the coupling of imaging techniques and numerical simulations, new challenges arise. One of them is to define an accurate and efficient technique for image segmentation, namely, determining to which physical phase each of the voxels belongs to. The objective of this work is to assess the influence of the image segmentation technique on the results of numerical simulations dedicated to ductile damage of nodular graphite cast iron.

Image segmentation is a well established field with a large number of methods adapted to different types of images and applications. These techniques range from medical applications [6] to quantification and analyses of porous microstructures [7]. Segmentation can be as simple as global thresh-

olding [8] or as complex as more recently developed techniques based on machine learning [9, 10].

One application in which the fields of image segmentation and mechanics have converged is the determination of mechanical properties of complex structures or microstructures [11, 3, 4, 12, 5]. This coupling provides an opportunity to better understand the relationship between microstructure and properties. For example, Madra et al. [11] analyzed qualitatively and quantitatively porosity in woven glass fiber reinforced composites via various segmentation methods. Another example is the study of complex metallurgical microstructures through pattern recognition techniques [12].

Although some studies have addressed the relevance of the employed segmentation method [7, 11, 12], the focus was generally restricted to the result of the segmentation step. The present work aims at assessing the effect of image segmentation up to its final use in the context of a micromechanical study of ductile damage applied to nodular graphite cast iron. More specifically, this work is dedicated to understanding and quantifying the effect of image segmentation on the final mechanical observables of interest (global stress and strain data, and local strains as well as void fraction and volume). If image segmentation introduces considerable uncertainty on the desired micromechanical quantities, these quantities cannot be used reliably. To the best of the authors' knowledge, this work constitutes the first effort of documentation and quantification of this problem.

Recently, an experimental-numerical framework was developed to study ductile fracture at the microscale. It is composed of three key techniques. First, three-dimensional images of specimens under load were acquired *in-situ* via Synchrotron Radiation Computed Laminography (SRCL) [13]. Second, Digital Volume Correlation (DVC) [14] enabled kinematic data to be measured from the registration of SRCL images. Last, Finite Element (FE) simulations with advanced meshing/remeshing techniques [15] were carried out on immersed microstructures and realistic boundary conditions extracted

from SRCL images via DVC analyses. This framework will be referred to as SRCL-DVC-FE, and was previously detailed in Ref. [3]. The importance of realistic boundary conditions was demonstrated with the SRCL-DVC-FE framework [4]. The measurement uncertainties of DVC applied to laminography data were evaluated, in particular, for cast iron [16]. The present work aims at assessing the uncertainties in the results of the FE simulations in the SRCL-DVC-FE framework that could be expected to originate from the segmentation of SRCL images.

The chosen mechanical quantities that result from simulations carried out with the SRCL-DVC-FE framework will be used in future works for calibrating void nucleation, growth or coalescence models. Relevant input is required for these tasks to be successful. For this reason, it is important to assess the magnitude of the uncertainty introduced during image segmentation.

Nodular cast iron is an engineering material of practical importance [17]. It is used in the transportation industry for railway wheels [18], for example, and in the energy industry for an important number of wind turbine parts [19]. Several works have been dedicated to the micromechanisms of ductile damage in nodular cast iron [20]. The sensitivity of crack growth rate to the distribution of particles in the process zone for materials with a high volume fraction of particles [21] illustrates the importance of studying real microstructures instead of idealized ones. In spite of this observation, even the most sophisticated numerical models for nodular cast iron found in the literature resort to at least some degree of idealization [22]. In this sense, the SRCL-DVC-FE methodology provides the opportunity to study immersed nodular cast iron microstructures subject to realistic boundary conditions. This is, however, a recent methodology and understanding the uncertainties in the chain of different employed techniques is necessary. Thus, the objective of this work is to understand and quantify the influence of image segmentation on the final FE results of simulations of immersed microstructures. This is of importance not only for the SRCL-DVC-FE methodology, but for any two-dimensional or three-dimensional numerical study of immersed

microstructures.

In order to assess the effect of the segmentation procedure in the results of the FE simulations within the SRCL-DVC-FE framework, three different established approaches are chosen (Section 2). They have to be able to deal with the measurement noise during image acquisition as well as with artifacts resulting from incomplete sampling of the 3D Fourier domain [23]. An additional criterion for the selection of the segmentation methods is their ability of being automated in the SRCL-DVC-FE chain of techniques, *i.e.*, the desired methods should be able to produce satisfactory results without requiring excessive fine-tuning of their intrinsic parameters. Micromechanical FE simulations are then carried out by immersing each of the segmented images and comparisons are made between the resulting predictions. This analysis has the objective of assessing the effect of image segmentation on the results of FE simulations of immersed microstructures. The comparisons have another practical consequence, namely, the uncertainty introduced during image segmentation of the results of the simulations can be estimated based on these comparisons. The comparative study and the subsequent uncertainty estimation are presented in Section 3.

2 Methodology

2.1 Material and specimen

A commercial nodular graphite cast iron is studied in this work. Its commercial code is EN-GJS-400. This material is of engineering importance and better understanding its damage mechanisms can have practical consequences [17, 18, 19, 20]. Additionally, it presents a high volume fraction of graphite nodules, which makes it attractive for DVC analyses [24]. DVC relies on the contrast in SRCL images due to microstructural heterogeneities, which is provided by the difference of X-ray absorption between the graphite

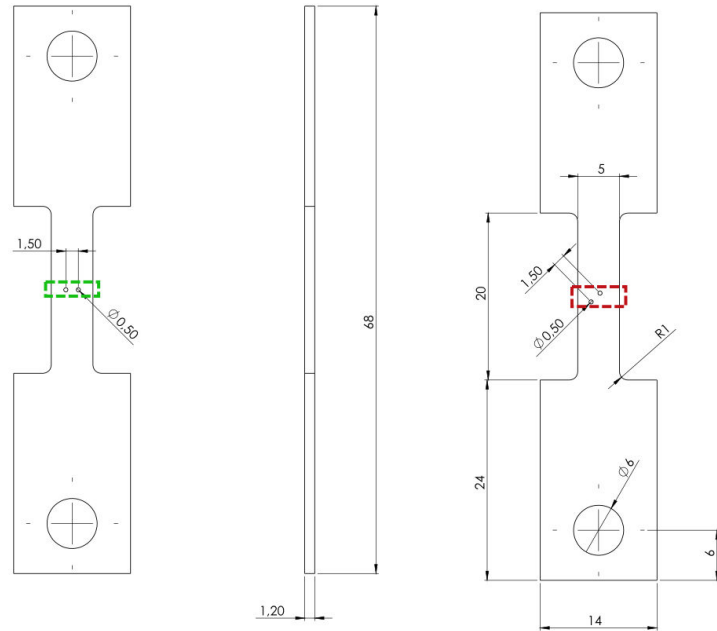
nodules and the ferritic matrix.

Two different specimens that were previously studied [25] are considered hereafter (Figure 1). Each of them contains two holes with a diameter of $500\ \mu\text{m}$ that were machined by Electrical Discharge Machining (EDM). The ligament connecting the centers of these two holes forms an angle of 90° with the loading direction in the first geometry, and 45° in the second geometry. Three-dimensional images were acquired via SRCL during *in-situ* tensile tests. Very early debonding between the graphite nodules and the ferritic matrix was observed in the mechanical tests. For this reason, and because the graphite nodules present a low load-bearing capacity [20, 26], the graphite nodules are considered as voids in the FE simulations. This hypothesis can have an influence on the results for large values of strain when void locking occurs.

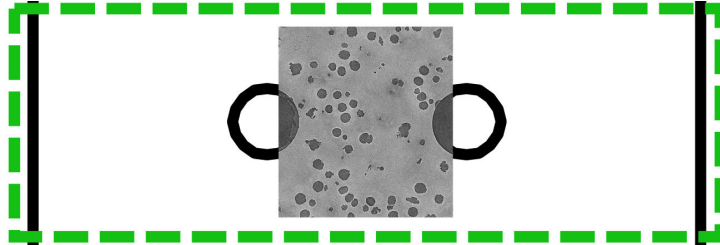
2.2 Image segmentation

Before immersing the microstructures in the FE mesh, it is necessary to differentiate the various phases in the 3D SRCL images of the reference configurations. This task is called image segmentation. In this work, image segmentation is conducted in FIJI [27], a distribution of the ImageJ software [28]. Three different image segmentation procedures are employed. Although each procedure consists of several operations, they will be referred to by the name of the defining method or algorithm. The first method, which is based on thresholding by inspection of the images, will be referred to as Thresholding. The second method employs an automatic thresholding procedure, and will be referred to as Automatic Thresholding. The third and last method, which is based on machine learning, will be referred to as Random Forest.

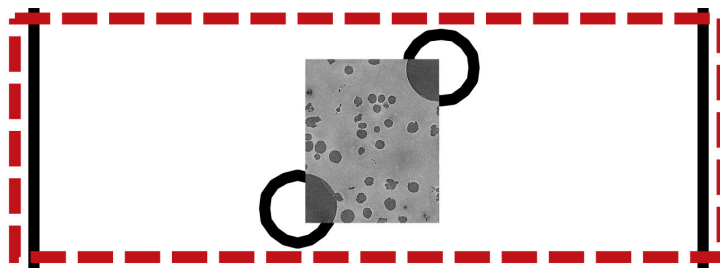
Other methods such as region-growth segmentation [29], fast marching algorithm and Level-set segmentation [30], were briefly tested. They were



(a)



(b)



(c)

Figure 1: (a) Geometry of the two studied specimens and zoom around the scanned region for the (b) 90° and (c) 45° specimens.

not selected since they required excessive user input or calibration, were very time-consuming, or provided unsatisfactory results.

Although entire slices of laminography images are presented, only the volume inside of the so-called reconstruction circle is subsequently used in the simulations. The reason is that information outside of this zone is incomplete [16] and hence not suitable for any quantitative analysis.

Ring artifacts are observed in the laminography images. The origin of these artifacts is related to the characteristic modulated intensity pattern of the cross-section of the beam. These modulations cause the manifestation of ring artifacts after reconstruction [16]. An additional requirement on the chosen segmentation methods is to be able of dealing with the presence of these artifacts.

2.2.1 Thresholding

Thresholding is a very simple segmentation operation that consists in determining the phase of a voxel based on its gray level, and it is particularly adapted for images where only two phases exist [8]. A unique thresholding by inspection was defined and applied to both specimens and will be illustrated only for the 90° specimen for the sake of brevity. This procedure involves four steps.

The first step consists of a three-dimensional averaging filter, *i.e.*, the gray level in a voxel is replaced with the average gray level in its immediate neighborhood. This operation results in smoother albeit coarser images. A mid-thickness slice of the 90° specimen is shown in Figure 2 in its original version (Figure 2a) and after applying the 3D-mean filter (Figure 2b).

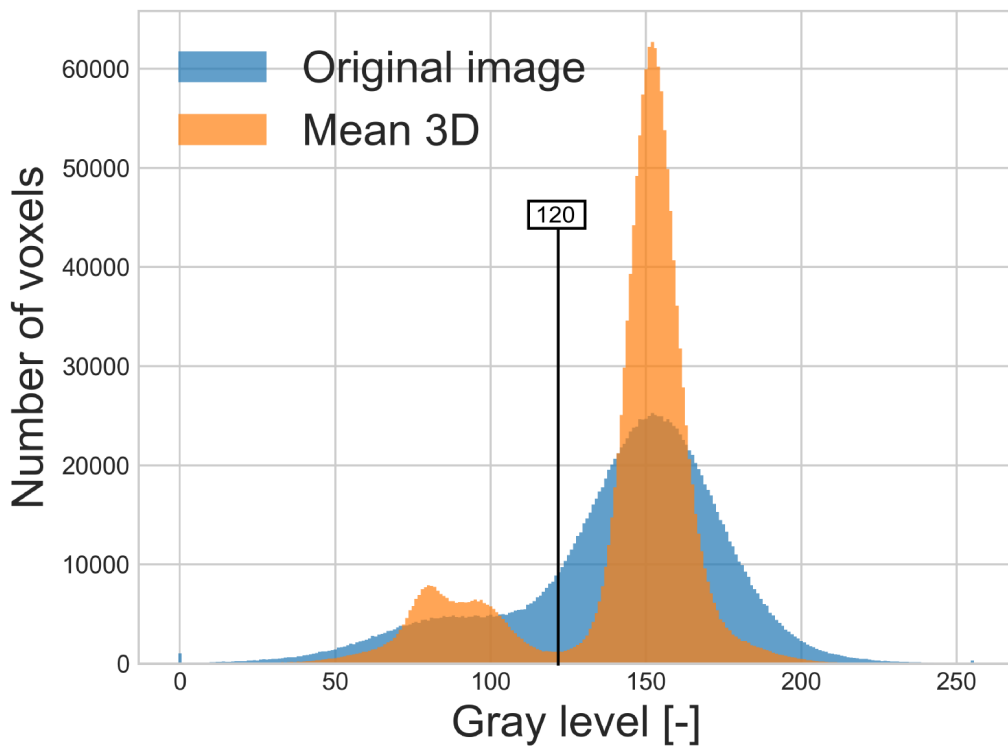
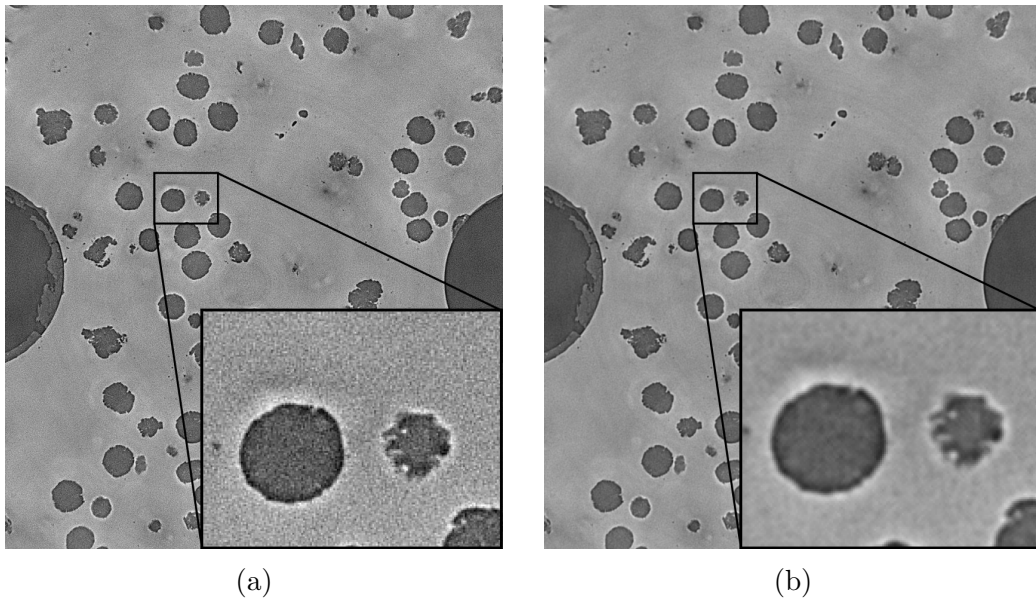


Figure 2: (a) Original slice at mid-thickness of the 90° specimen, and (b) after applying the 3D-mean filter. (c) Corresponding gray level histogram of the original image and after applying the 3D-mean filter. The 120 gray level defines the segmentation threshold between the nodules and the ferritic matrix.

The effect of the increased smoothness on the gray level histogram is illustrated in Figure 2c. The gray level histogram of the original image is bimodal and presents considerable overlap between the two superimposed distributions. This makes the original image difficult to segment through simple thresholding. Applying the 3D-mean filter has the effect of reducing the spread of each of the superimposed distributions. Choosing a reasonable threshold is thus possible. The chosen value was 120 for both images.

Buljac et al. [25] proposed another methodology for reducing the subjectivity in the choice of the threshold. It consisted in using the strain tensor trace obtained from DVC analyses to obtain void growth during the *in-situ* test, and comparing this history with the void growth obtained via segmentation of the 3D images with different thresholds. The chosen threshold was then the one that better matched the void growth evaluated with the strain tensor trace (*i.e.*, 115). Although in the current work the threshold was determined by simple inspection of the images and their gray level histogram, it is close to that chosen by Buljac et al. [25].

The result of the thresholding procedure is illustrated in Figure 3a. Figure 3b shows the final segmented image after applying two additional filters. The first one carries out a fill-hole operation to eliminate white voxels within voids. The second (median) filter is typically used to eliminate salt-and-pepper noise. It is applied to remove isolated black voxels in the matrix (Figure 3b).

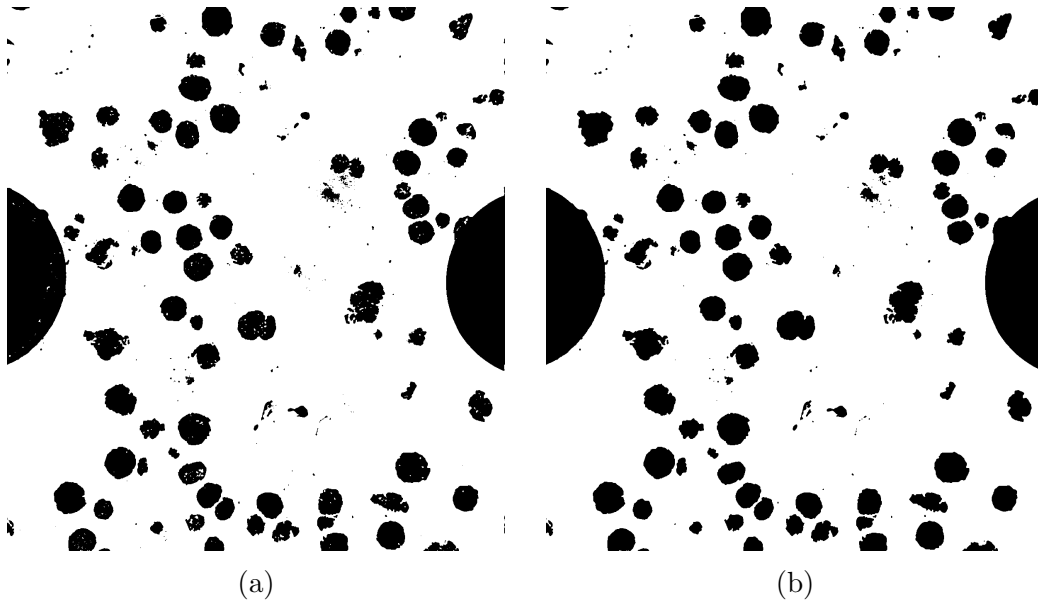


Figure 3: Slice at mid-thickness of the 90° specimen after (a) thresholding, and (b) applying the fill-hole and despeckle filters.

2.2.2 Automatic thresholding

A segmentation procedure with an automatic thresholding technique is described in this section. It is carried out in three steps. First, Gaussian blur with standard deviation of 5 voxels is applied to the original image. The automatic thresholding technique is then applied, and finally, a fill-hole operation is performed.

Gaussian blur accomplishes the same function as the 3D-mean filter applied in the manual thresholding procedure (see Section 2.2.1). The objective of this work is not to carry out a detailed comparison of different segmentation methods under the same condition. The deliberate choice of different preprocessing steps before the segmentation helps emphasizing the effect of the human factor in the entire segmentation procedure.

The automatic thresholding algorithms that are available in FIJI were

evaluated on the mid-thickness slice of the 45° specimen, and the results are summarized in Figure 4. The tested techniques are, in order of appearance, the IsoData algorithm [31], Huang’s fuzzy thresholding method [32], the Intermodes method [33], a second implementation of the IsoData algorithm, an iterative version [34] of Li’s Minimum Cross Entropy method [35], a Maximum Entropy method [36], using the mean of the gray levels as a first guess for the threshold value [37], an iterative version of the Minimum Error method [38], the so-called Minimum method with histogram smoothing [33], the moment-preserving method [39], the clustering algorithm [40], the so-called Percentile method, which assumes a given fraction of foreground voxels (0.5 by default) [41], the Maximum Entropy method with Renyi’s entropy [42], the Information Measure method [43], the Triangle method [44], and the automatic multilevel method [45].

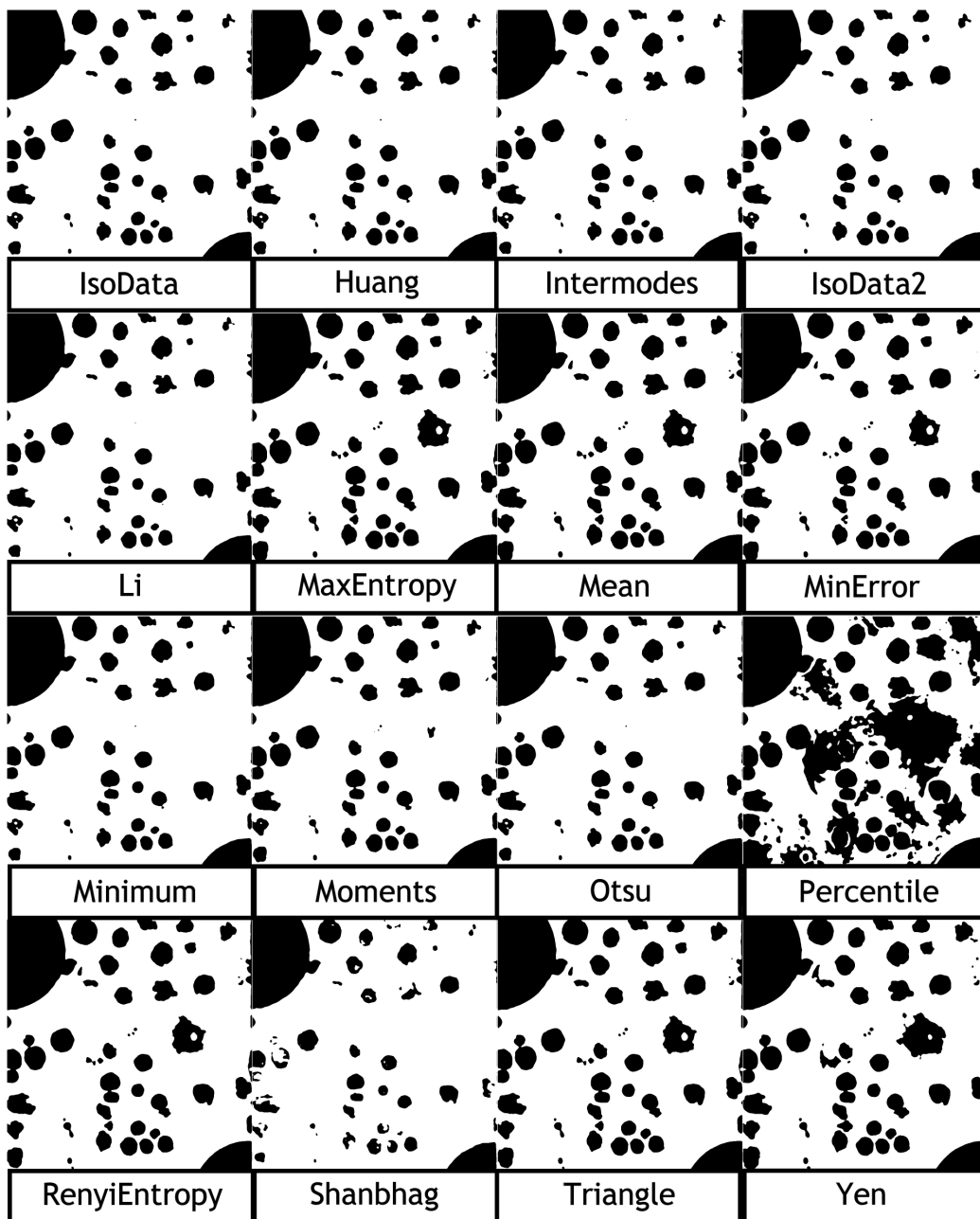


Figure 4: Mid-thickness slice of the 45° specimen segmented with different automatic thresholding methods.

The results of the employed automatic thresholding techniques reported in Figure 4 were qualitatively examined through comparison with the original

image (Figure 7c). Similar and satisfactory results were provided by both IsoData methods, Huang’s method, the Intermodes method, Li’s method, the Minimum method, and Otsu’s method. The IsoData algorithm was selected because of its simplicity and applied for segmenting the 3D images of both specimens.

The iterative IsoData algorithm classifies the voxels into two categories with an initial threshold value, and the average gray level of each category is calculated. The average of the latter is then proposed as a new threshold until convergence. The algorithm was applied separately for each slice, *i.e.*, a threshold value was calculated for each individual slice of the volumetric images. This choice was made to be consistent with the Random forest procedure which is too costly to be applied to the whole 3D image.

2.2.3 Random forest procedure

The random forest procedure is based on machine learning [46], and involves two steps, namely, training and classification. A random forest is a machine learning classification method in which many decision trees vote and the resulting most popular category is retained. A decision tree is a simpler classification model that consists of nodes and branches. The initial node is the root and the terminal nodes are denoted as leafs. Each node, except for leafs, represents a test and each subsequent branch corresponds to the result of a test. The classification ends at the leafs, which contain the label of a class. In this work, the classes are either void or matrix. An example of a possible decision tree for a given voxel is schematized in Figure 5. The depicted tree uses two training features, namely, the gray level and the first principal curvature.

After classification, fill-hole and median filters were also applied. During training, a classification model was created. The data used for training were the mid-thickness slice of the specimen, and twenty freehand traces were

chosen for each of the two classes (*i.e.*, matrix and voids). The training features were Gaussian blur, Sobel and Hessian filters, difference of Gaussians and membrane projections.

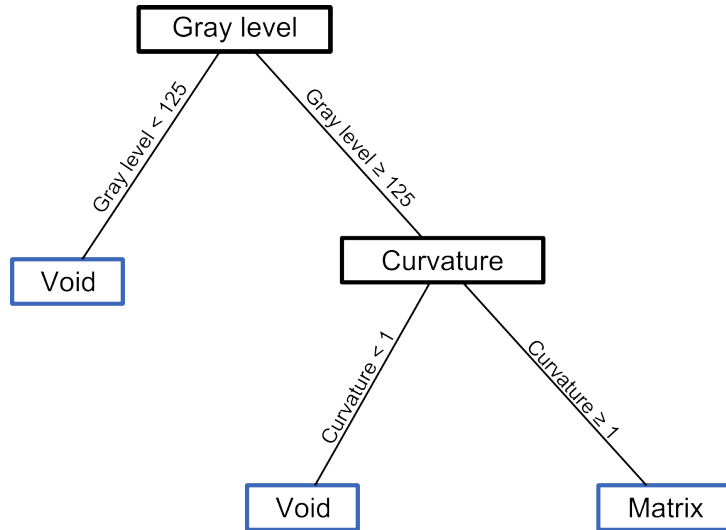
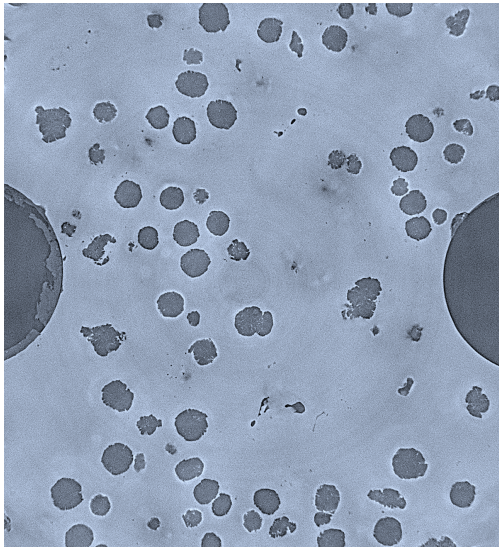


Figure 5: Example of a possible decision tree for a voxel with two features (gray level and first principal curvature).

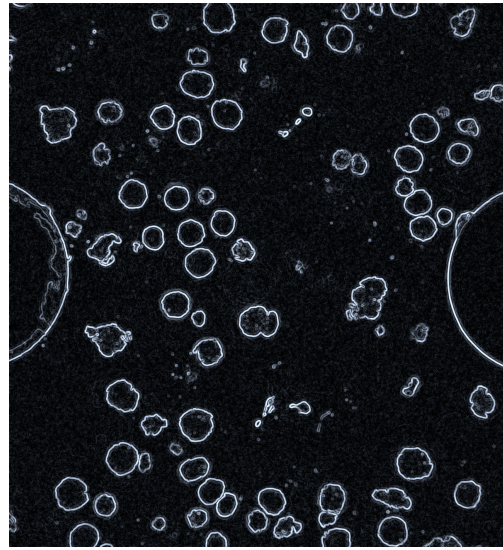
Five Gaussian (blur) filters, with different standard deviations ranging from 1 to 16 voxels, were used. The Sobel filter provides an approximation of the gray level derivative and helps locating interfaces. Information on the curvature of the interfaces is provided by the Hessian filter. The difference of Gaussians filter is useful for blob detection due to laminography artifacts or the nearby presence of voids in the thickness direction. Membrane projections may provide additional information on the location of boundaries. More information on these filters can be found in the documentation of the Weka Trainable Segmentation library [47].

The use of filters and their combinations provide a total of 76 training features. Three of these features are exemplified in Figure 6 along with the original image (Figure 6a) for the slice at mid-thickness of the 90° specimen. Figure 6b shows the result of applying the Sobel filter after Gaussian blur with a standard deviation of 4 voxels. This operation highlights the

void/matrix interfaces. Figure 6c shows the square difference of the first and second eigenvalues of the Hessian after Gaussian blur with a standard deviation of 16 voxels, *i.e.*, the high curvature zones are determined. Ring-shaped artifacts are brought into evidence with a lesser curvature than the contour of the voids. Membrane projections with the mean of the voxels provides a marginal enhancement of the interfaces and an overall smoothing of the image.



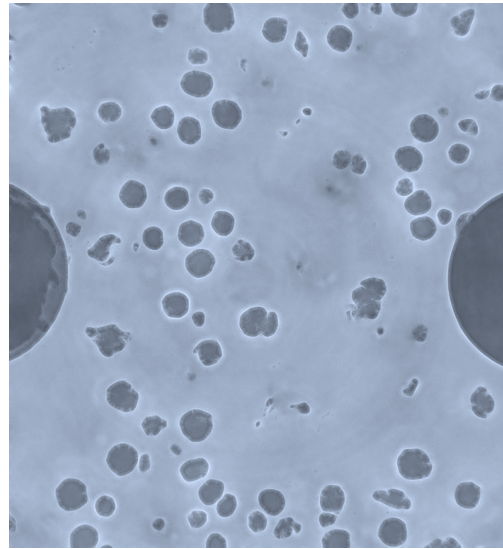
(a) Original image



(b) Sobel filter



(c) Hessian filter



(d) Membrane filter

Figure 6: Original mid-thickness slice of the 90° specimen, and the result of applying three different filters to the same slice.

Two features per tree and 200 trees were used in the classification stage. A classifier model for each of the specimen was created. The original and classified images for the slice at mid-thickness of the 90° and 45° specimen

are shown in Figure 7.

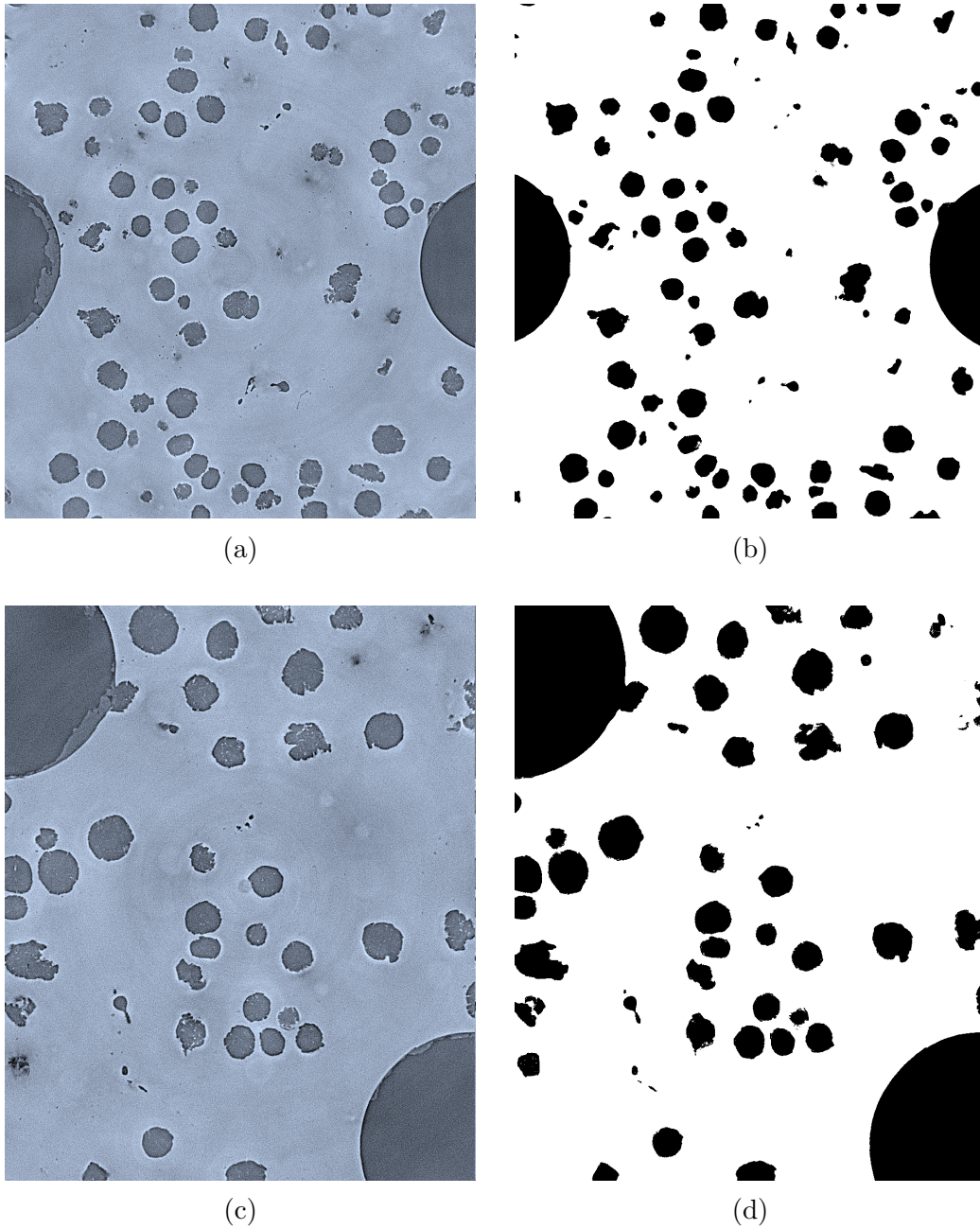


Figure 7: Original slice at mid-thickness of the (a) 90° and (c) 45° specimens and the same slice after classification with the random forest procedure. for the (b) 90° and (d) 45° specimens.

2.3 Numerical simulations

The experimental-numerical SRCL-DVC-FE framework developed by Buljac et al. [3, 4] is used in this work to carry out micromechanical FE simulations of immersed microstructures and realistic boundary conditions. The key ingredients of this methodology are the acquisition of tomographic or laminographic images during *in-situ* tests, the measurement of 3D kinematic fields via DVC, and FE modeling of the immersed microstructures using measured displacements as Dirichlet boundary conditions. A simple schematic diagram of the SRCL-DVC-FE framework is presented in Figure 8.

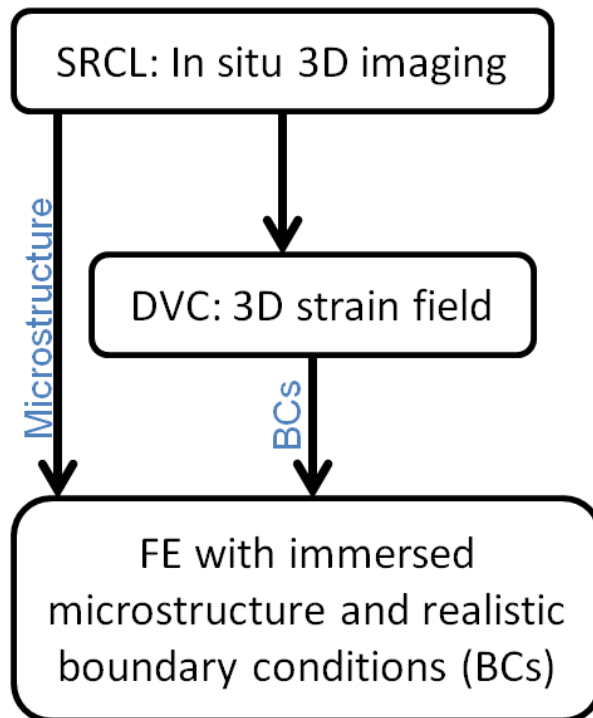


Figure 8: Schematic flowchart of the SRCL-DVC-FE framework.

DVC provides three dimensional displacement fields. These heterogeneous displacement fields are interpolated onto the boundaries of the FE domain, and applied as Dirichlet boundary conditions at each loading step [4]. Each loading step constitutes an increment for the FE simulations. A man-

ual testing device is used to apply a displacement via screw rotation. The corresponding screw displacements are summarized in Table 1.

Table 1: Screw displacement applied to each of the specimens.

Increment	Screw displacement [μm]	
	45° specimen	90° specimen
0	0	0
1	248	186
2	372	248
3	496	289
4	620	330
5	744	372
6	868	413
7	992	454
8	1074	496
9	1136	537
10	1198	578
11	1260	599
12	-	620
13	-	641
14	-	661
15	-	682
16	-	703
17	-	722
18	-	744
19	-	765

In the SRCL-DVC-FE framework, a distance function describes the position of the void-matrix interface. Excellent conservation of the volume of the void phase is ensured by the use of body-fitted meshing and remeshing operations with an appropriate treatment of coalescence events [15]. Curvature-based mesh adaption is employed in this work [48]. An isotropic metric \mathbf{M} is built with the maximum principal curvature λ_{max} [49]

$$\mathbf{M} = \text{diag} \left(\frac{1}{h^2} \right), \quad (1)$$

where h is the mesh size. The mesh size is calculated as

$$h = \max \left(\min \left(\frac{h_c}{\lambda_{max}} + \left(h_{max} - \frac{h_c}{\lambda_{max}} \right) \frac{\phi}{\epsilon_h}, h_{max} \right), h_{min} \right), \quad (2)$$

where h_c corresponds to the mesh size that would be prescribed if $\lambda_{max} = 1$, h_{min} and h_{max} are the smallest and largest allowed mesh sizes respectively, ϕ the distance function of the void phase, and ϵ_h a fixed user-controlled thickness along which the mesh size varies linearly from $\frac{h_c}{\lambda_{max}}$ to h_{max} .

Monolithic multiphase FE simulations were conducted with a Lagrangian formulation in the CimLib library [50] with a P1+/P1 formulation [51]. The term monolithic refers to the solution of the governing equations with a *single* mesh and a global framework for all of the present phases. This approach was documented in previous works [52, 15], and only some general aspects are recalled hereafter. Since the graphite nodules present very early debonding and have a very low load-bearing capacity [20, 26], they will be considered as voids in the FE simulations. The term ‘void’ will thus be used to refer to the volume corresponding to the nodules and actual voids. This hypothesis has been adopted and validated in a previous work [3].

The matrix is considered to be elastoplastic with Ludwik’s isotropic hardening law

$$\sigma_{eq} = \sigma_y + K \varepsilon_{pl}^n, \quad (3)$$

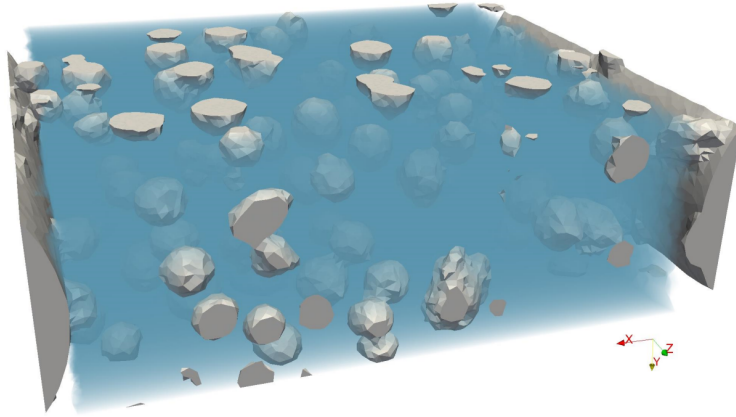
where σ_{eq} is the von Mises equivalent stress, ε_{pl} the cumulated plastic equivalent strain, σ_y the yield stress, K the hardening modulus and n the hardening exponent. The employed values for the Young’s modulus E , and Poisson’s ratio ν were $E = 210$ GPa, and $\nu = 0.3$. The values for σ_y , K , and n were previously calibrated at the microscale by means of X-ray microtomography, DVC, and FE simulations [5], namely, $\sigma_y = 245$ MPa, $K = 330$ MPa, and $n = 0.21$. The void phase is modeled as a compressible Newtonian fluid with viscosity $\eta = 2.1$ MPa s⁻¹. This viscosity value is chosen after a sensitivity analysis to ensure that the stress levels induced in the matrix are negligible. This approach facilitates handling the void phase in the present monolithic

framework and it has been previously used and validated [53].

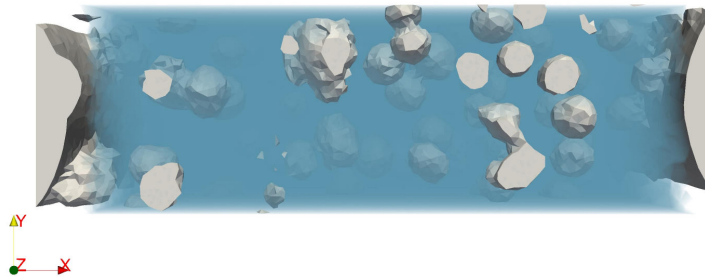
The FE domain is contained in the Region Of Interest (ROI) analyzed via DVC. This is done so to ensure that boundary conditions are available during the whole simulation [3]. The largest domain that provides boundary conditions for all of the available DVC increments is chosen.

2.4 Observables

Global and local quantities were considered for each specimen. The global information was calculated in the whole domain for the 45° specimen and in a fraction of the domain for the 90° specimen. The purpose of the latter choice is to exclude the EDM-machined holes from the global calculation since they lie partially inside of the domain for the 90° specimen, and would have led to inaccurate void volume quantification. The domain for the calculation of the global quantities in the 90° specimen is shown in Figure 9 as a semi-transparent blue volume. The term global volume will be used to make reference to the whole domain in the case of the 45° specimen simulation, and to the volume depicted in Figure 9 for the 90° specimen.



(a)



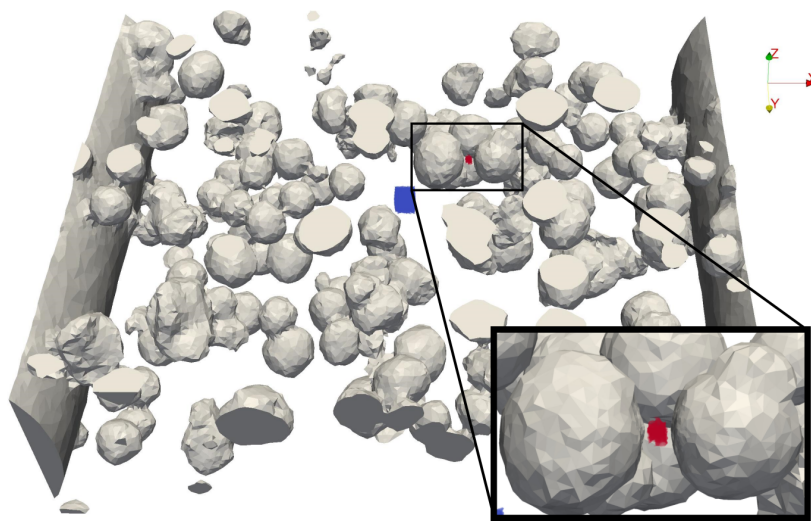
(b)

Figure 9: Two different views of the domain for the 90° specimen simulation. The domain where the global quantities are calculated is shown as a semi-transparent blue volume. Voids are shown in gray.

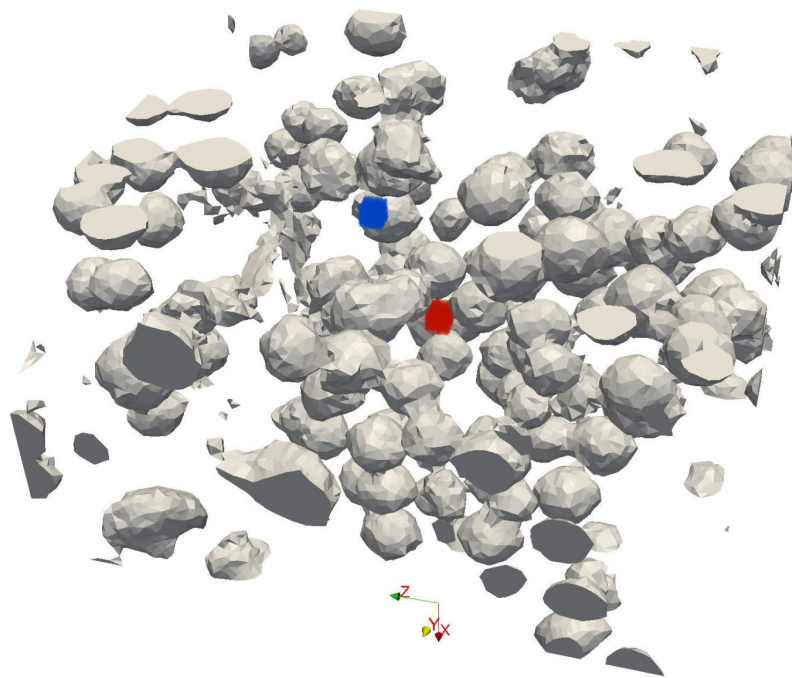
The global observables are the volume-averaged (or macroscopic) von Mises equivalent strain, the (macroscopic) von Mises equivalent stress, the void volume fraction, and void growth. The latter is defined as the ratio between the current void volume and the initial void volume.

Additionally, the volume-averaged equivalent strain in two local probes per specimen is assessed. The local probes are displayed as a blue cube (probe 1) and as a red cube (probe 2) in Figure 10a for the 90° specimen, and in Figure 10b for the 45° specimen. The positions of the probes are

exactly the same as those analyzed by Buljac et al. [25]. These volumes enable for the study of void coalescence by ligament failure. The probe volume corresponds, except for probe 2 of the 90° specimen, to that of C8 elements with an edge of 35 μm , in DVC calculations. The size of probe 2 of the 90° specimen had to be reduced to 1/16th of the volume of the other probes so that it could fit in the intervoid ligament without being in contact with the voids. The initially cubic shape of the probes corresponds to the DVC elements, and evolves with deformation, *i.e.*, the probed volumes are Lagrangian.



(a)



(b)

Figure 10: 3D view of the computational domain for the (a) 90° specimen and (b) the 45° specimen. Local probes are shown in blue (probe 1) and red (probe 2). A local zoom displays probe 2 of the 90° specimen.

A total of six observables per specimen will be assessed and were chosen in accordance with future work related to experimental-numerical comparisons as well as parameter identification of macroscopic damage laws.

3 Results

The results of a mesh sensitivity analysis are first presented for all of the considered observables and both specimens. A comparison of the predictions of the three segmentation procedures is reported in terms of their effect on the observables. Finally, an uncertainty estimation method is proposed.

3.1 Mesh sensitivity analysis

In addition to the curvature-based mesh adaption described in Section 2.3, an additional local refinement was carried out around the probes to ensure mesh-independent local values without significantly increasing the computational cost with further global refinement. The isotropic mesh size h was forced to take the value $h = \frac{h_{min}}{4}$ (see Equation (2)) in the probe and its surroundings. This extended locally refined volume was constructed by adding $2h_{min}$ to the distance function that describes the probes. The local refinement is illustrated for probe 1 of the 45° specimen in Figure 11.

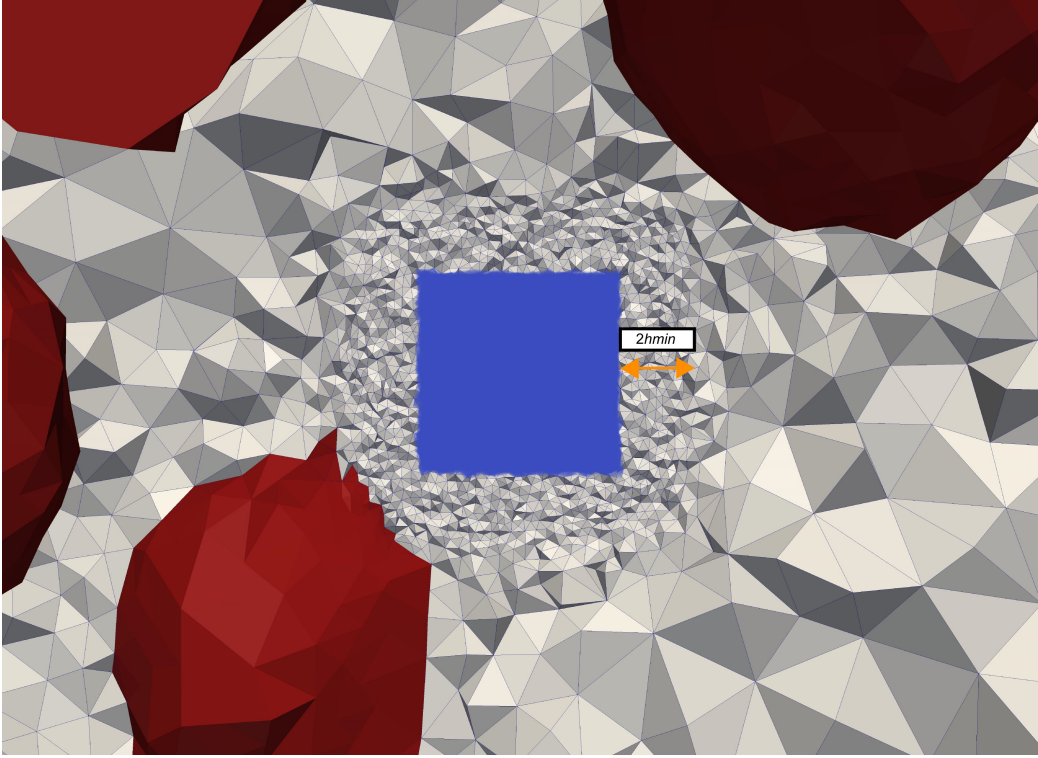


Figure 11: Probe 1 (in blue) in the 45° case with the mesh in a 2D slice of the domain showing the local refinement. The extended refined volume around the probe is indicated in orange. The voids are shown in red.

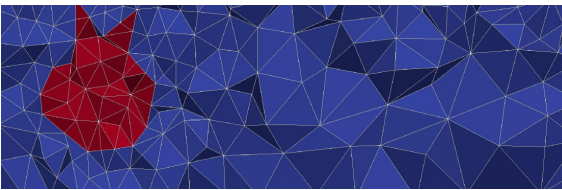
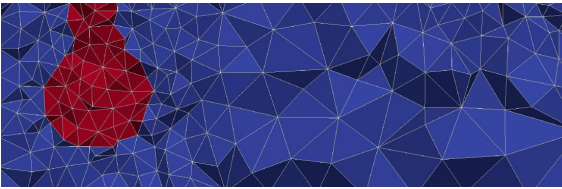
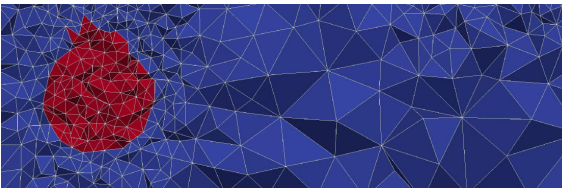
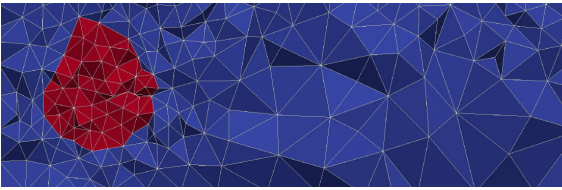
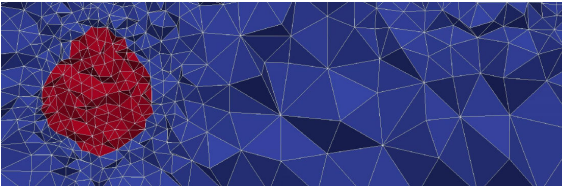
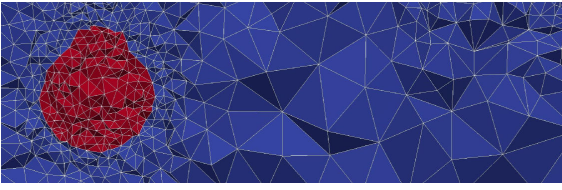
To simplify the mesh sensitivity analysis, two scaling factors F_1 and F_2 are introduced. The first one, F_1 , multiplies h_c , h_{min} and h_{max} , while the second one, F_2 , multiplies h_c and h_{min} . The values of the original mesh parameters are set to $h_c = 2.5 \times 10^{-3} \mu\text{m}$, $h_{min} = 2.5 \times 10^{-1} \mu\text{m}$, and $h_{max} = 5 \mu\text{m}$. When the scaling factors are introduced, the mesh size is calculated as

$$h = F_1 \max \left(\min \left(\frac{h_c F_2}{\lambda_{max}} + \left(h_{max} - \frac{h_c F_2}{\lambda_{max}} \right) \frac{\phi}{\epsilon_h}, h_{max} \right), h_{min} F_2 \right). \quad (4)$$

The effect of F_1 is straightforward, namely, modifying F_1 is equivalent to scaling the calculated mesh size h . The effect of F_2 is slightly more subtle. When F_2 decreases, the mesh size close to the interfaces decreases, but the maximum mesh size far away from the interfaces is unchanged. This effect

results in an increased mesh size gradient. Table 2 summarizes the effect of F_1 and F_2 parameters for the 45° specimen for different combinations.

Table 2: Mesh parameters and corresponding number of elements for the 45° specimen. A close-up view of a slice of the mesh is shown for each case. The matrix is shown in blue and voids in red.

Case	F_1	F_2	Number of elements	Mesh
1	4	4	424,806	
2	3	4	749,875	
3	2	4	1,706,833	
4	4	3	753,754	
5	4	2	1,685,267	
6	4	1.5	2,968,499	

3.1.1 Effect of F_1

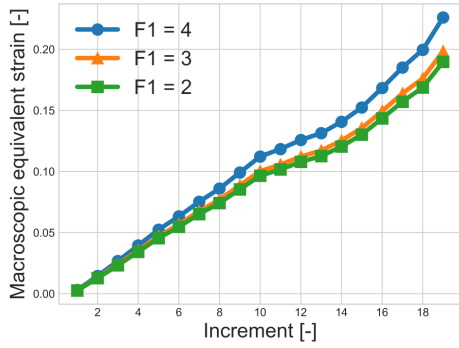
Simulations were carried out using meshes with three different F_1 values (*i.e.*, $F_1 = 4$, $F_1 = 3$ and $F_1 = 2$). Decreasing F_1 is equivalent to carrying out a global mesh refinement.

90° specimen

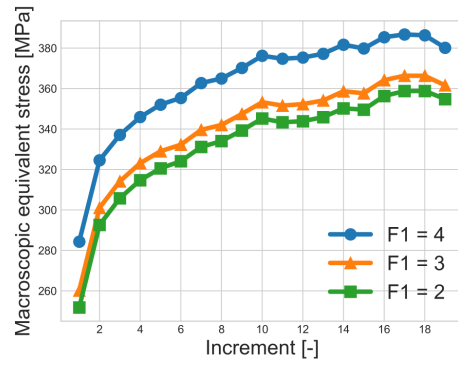
In the case of the 90° specimen, the results are shown in Figure 12 for the six observables. All observables seem to approach mesh independence as F_1 decreases, *i.e.*, the gap between the results with $F_1 = 2$ and $F_1 = 3$ is smaller than that when $F_1 = 3$ and $F_1 = 4$. The most sensitive variables are the macroscopic equivalent stress (Figure 12b) and the void volume fraction (Figure 12c). The void volume fraction presents significant differences since the microstructure cannot be described properly by a coarse FE mesh. As the mesh size decreases, the microstructural features are better described. The small decrease of the equivalent strain in probe 2 for the coarsest mesh in the last increment is caused by numerical diffusion of the probe volume during remeshing operations, *i.e.*, this mesh is not fine enough to appropriately handle numerical diffusion.

45° specimen

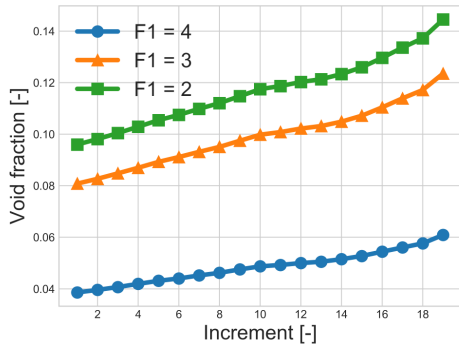
The effect of varying F_1 is shown in Figure 13 for the the six observables. Contrary to the simulation of the 90° specimen, an unexpected response is found for the 45° specimen when F_1 is varied. The gap between the results with $F_1 = 2$ and $F_1 = 3$ is greater than that between $F_1 = 3$ and $F_1 = 4$. The reason for this trend is that there are microstructural features that the meshes with $F_1 = 3$ and $F_1 = 4$ are too coarse to capture. This explanation is consistent with the trend followed by the void volume fraction (Figure 13c) and the macroscopic equivalent stress (Figure 13b). When F_1 decreases,



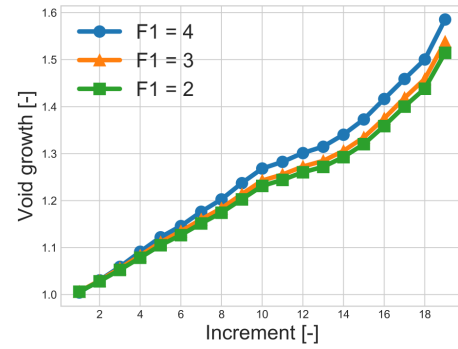
(a)



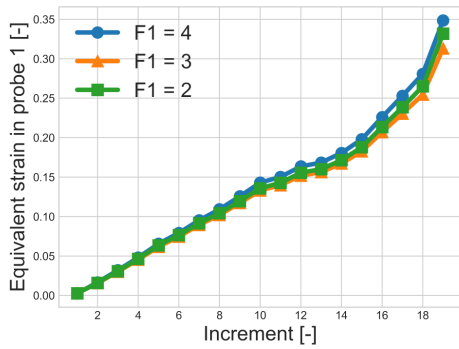
(b)



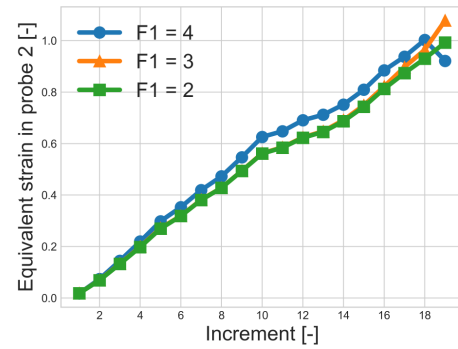
(c)



(d)



(e)



(f)

Figure 12: Mesh sensitivity in terms of F_1 for (a) macroscopic equivalent strain, (b) macroscopic equivalent stress, (c) void volume fraction, (d) void growth, and equivalent strain in (e) probe 1 and (f) probe 2 in the 90° specimen.

the mesh is able to capture smaller voids, as well as the shape of the bigger voids. Hence, the void volume fraction increases, and the loss of load-bearing capacity induces a decrease in the macroscopic equivalent stress.

The equivalent strain in probe 1 barely changes when the mesh size decreases (Figure 13e). In probe 2, however, when $F_1 = 2$, the equivalent strain experiences an unexpected and significant decrease (Figure 13f). The reason for this effect is that this mesh captures microstructural features that coarser meshes could not, and these features modify the local heterogeneous partition of strain in the vicinity of probe 2. This is illustrated in Figure 14 at increment 11 in the slice of the computational domain that contains the center of probe 2 for $F_1 = 4$ (Figure 14a) and $F_1 = 2$ (Figure 14b). Although the general strain distribution is similar for both meshes, local differences in topology and strain distribution are observed at different locations including the position of probe 2.

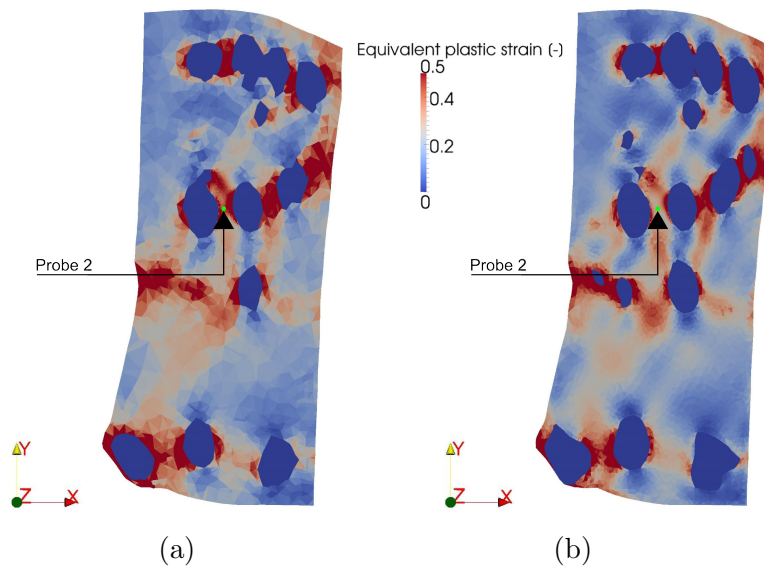
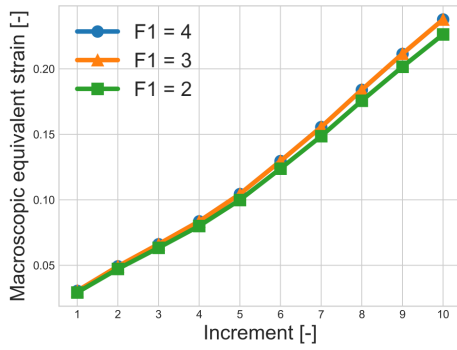
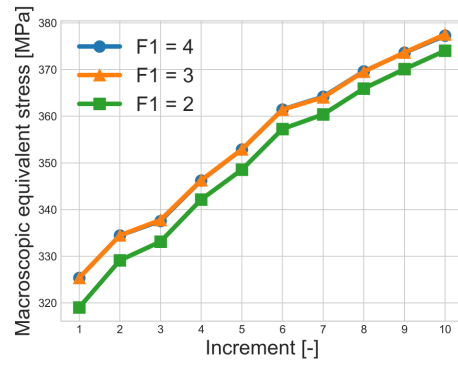


Figure 14: Strain distribution at increment 11 in the slice of the computational domain that contains the center of probe 2 for the 45° specimen for (a) $F_1 = 4$ and (b) $F_1 = 2$.

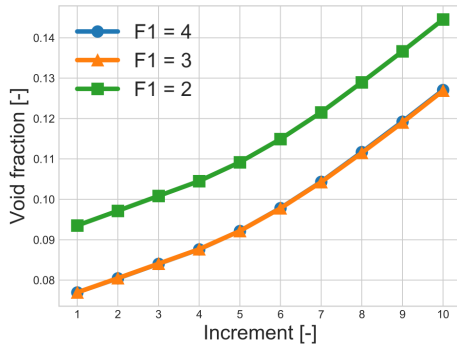
The mesh sensitivity of the void volume fraction in the 90° specimen sim-



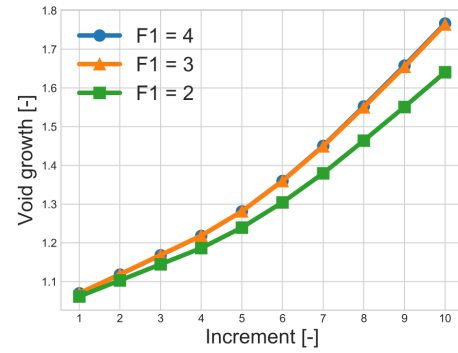
(a)



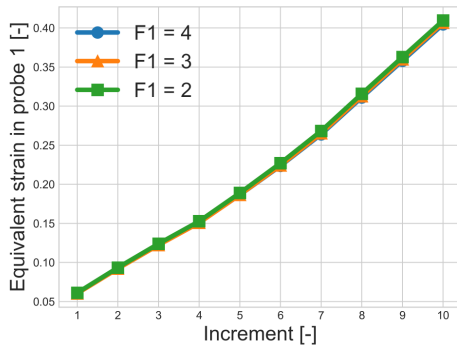
(b)



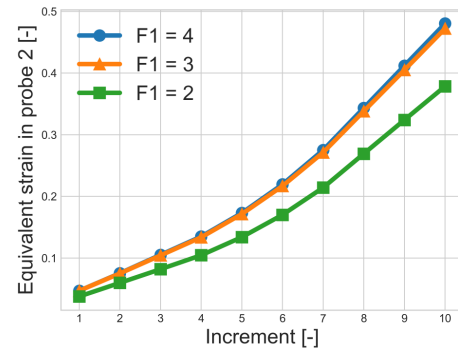
(c)



(d)



(e)



(f)

Figure 13: Mesh sensitivity in terms of F_1 for (a) macroscopic equivalent strain, (b) macroscopic equivalent stress, (c) void volume fraction, (d) void growth, and equivalent strain in (e) probe 1 and (f) probe 2 in the 45° specimen.

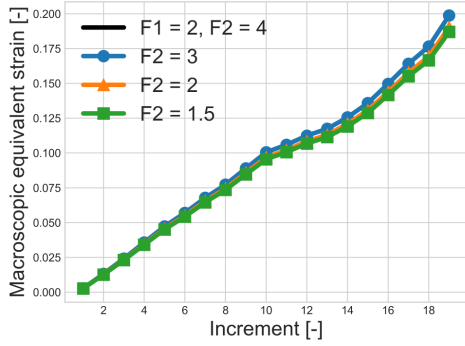
ulation is too substantial to consider that convergence was achieved. For the 45° simulation, verification of mesh independence is inconclusive because of the unexpected behavior found when F_1 is decreased for the void volume fraction as well as for the strain in probe 2. For these two reasons, it is desirable to extend the mesh verification analysis. However, further refinement of the mesh with a decrease of F_1 is very costly. A different strategy is adopted and described in Section 3.1.2.

3.1.2 Effect of F_2

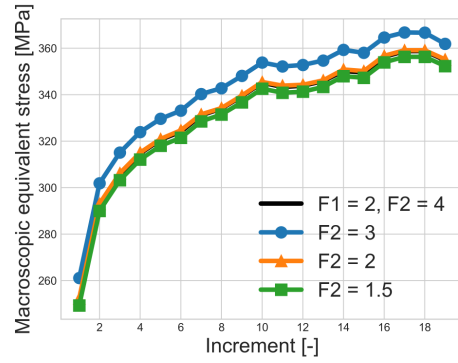
To extend the sensitivity analysis, the effect of varying F_2 is assessed in this section. Decreasing F_2 results in a better description of the interfaces while retaining a fixed mesh size far from them, i.e., this strategy aims at providing a satisfactory description of the geometry while decreasing as much as possible the computational cost. A fixed value of $F_1 = 4$ is used and results for $F_2 = 3$, $F_2 = 2$, and $F_2 = 1.5$ are presented. As a reference to the analysis in Section 3.1.1, the results with $F_1 = 2$ and $F_1 = 4$ are included in the figures as a black solid line.

90° specimen

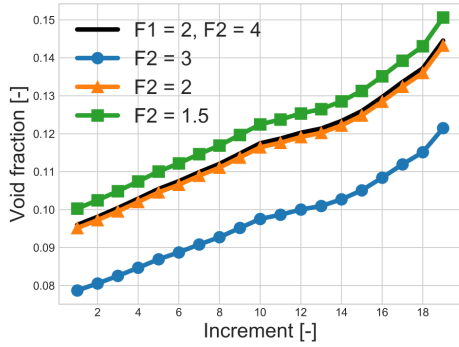
The effect of varying F_2 in the 90° simulation is illustrated for the six observables in Figure 15. All observables seem to approach mesh convergence as F_2 decreases. The curves with $F_2 = 2$ match very well those when $F_1 = 2$. In general, when F_2 is further decreased to F_1 , the resulting curves stay satisfactorily close to those corresponding to $F_2 = 2$. The void volume fractions remain the most sensitive observable and the variation it undergoes when F_2 decreases from 2 to 1.5 is not negligible.



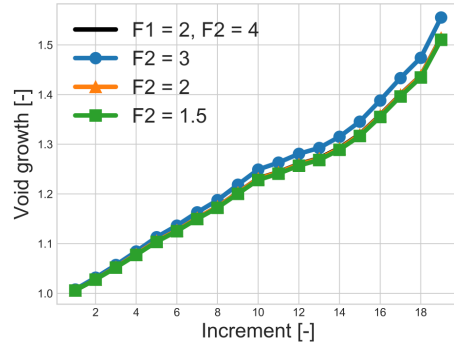
(a)



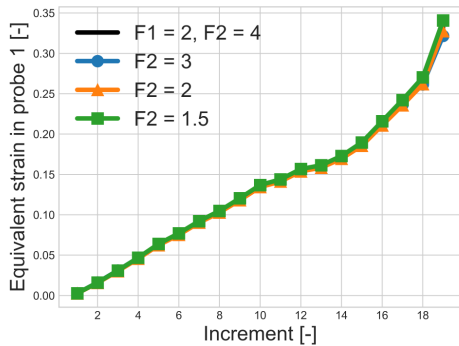
(b)



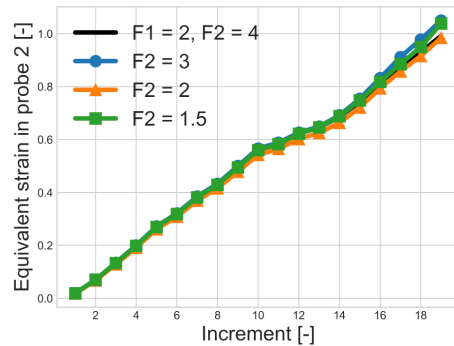
(c)



(d)



(e)



(f)

Figure 15: Mesh sensitivity in terms of F_2 for (a) macroscopic equivalent strain, (b) macroscopic equivalent stress, (c) void volume fraction, (d) void growth, and equivalent strain in (e) probe 1 and (f) probe 2 in the 90° specimen.

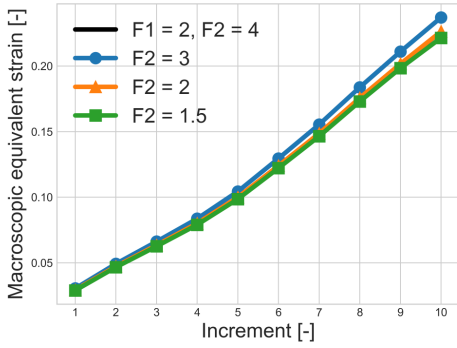
45° specimen

The sensitivity of the observables for the 45° simulation when F_2 is varied is shown in Figure 16. For all observables in the 45° simulation, the trend is the same as for the 90° specimen, namely, the gap between two successive curves decreases monotonically as F_2 decreases. In this case too, the curve with $F_2 = 2$ matches very well the reference curve with $F_1 = 2$. The observable most sensitive to the mesh is again the void volume fraction.

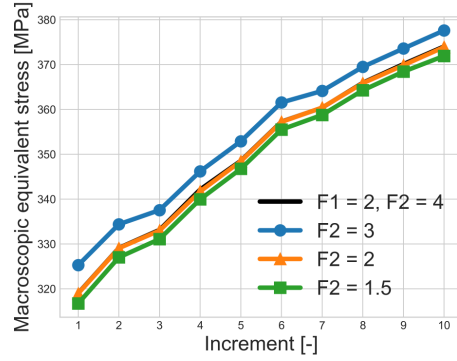
Although the results are satisfactory for most of the observables, given the acceptably small yet non-negligible variations exhibited by the void volume fraction for the simulations of both specimens, further refinement could be considered. The associated computational costs would make further refinement impractical, and more importantly, attention must be paid to the relative order of magnitude of the minimum mesh size with respect to resolution of the laminography images. For example, for the finest employed mesh with $F_1 = 4$ and $F_2 = 1.5$, the resulting minimum allowed mesh size is $1.5 \mu\text{m}$, which is of the same order of magnitude of the laminography resolution with cubic voxels of edge length $1.1 \mu\text{m}$ [3]. The mesh with $F_1 = 4$ and $F_2 = 1.5$ is selected for the remainder of the study.

3.2 Model cross comparison

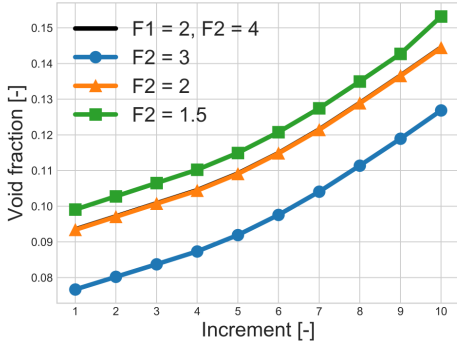
For the random forest procedure, a simple training procedure was carried out on a single slice for each specimen. However, the training stage is critical and can be tedious in more complex cases. For this reason, it would be convenient to be able to train a single classifier model in a chosen image and subsequently use the model in other images of similar features. To explore the feasibility of reusing a model in different specimens, a cross comparison is carried out. There are two factors that can play an important role in the comparison, namely, the criterion of the operator who trained the models, and differences between images due to, for example, the variation in beam



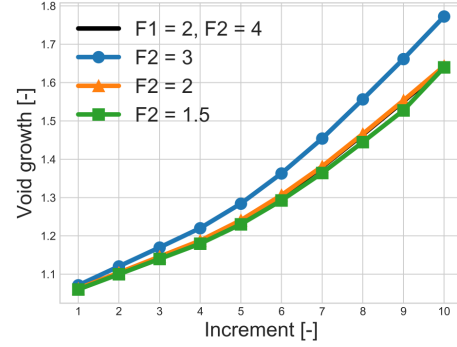
(a)



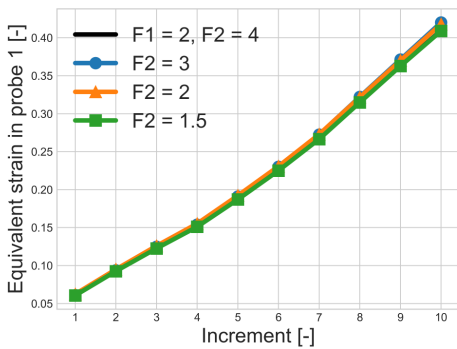
(b)



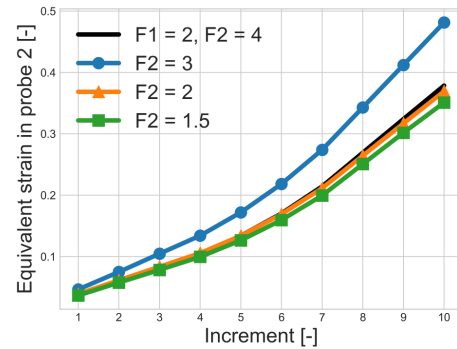
(c)



(d)



(e)



(f)

Figure 16: Mesh sensitivity in terms of F_2 for (a) macroscopic equivalent strain, (b) macroscopic equivalent stress, (c) void volume fraction, (d) void growth, and equivalent strain in (e) probe 1 (f) probe 2 in the 45° specimen.

intensity during laminography acquisitions.

Two simulations were carried out for each specimen, namely, one with the model created for the same specimen, and one with the model created for the other specimen. The results of the comparison between each pair of simulations are reported in Figure 17 (90° specimen) and Figure 18 (45° specimen). Additionally, an absolute difference calculated with respect to the smallest of two compared quantities is reported for each observable.

The comparison for both specimens leads to similar results. The maximum absolute difference for the macroscopic equivalent strain, macroscopic equivalent stress, and for the equivalent strain in probe 1, is of the order of or less than 3×10^{-3} . The void growth has a maximum absolute difference of 1.5×10^{-2} for the 90° specimen and of approximately 3.5×10^{-2} for the 45° specimen. The void volume fraction is less sensitive in terms of absolute differences. A maximum absolute difference of 6.2×10^{-3} was obtained for the 90° case, and 4.2×10^{-3} for the 45° sample.

The equivalent strain in probe 2 exhibits a maximum absolute difference of 9×10^{-3} for the 45° simulation. For the 90° simulation, probe 2 is very sensitive since a maximum absolute difference of approximately 8×10^{-2} is noted. The increased sensitivity of probe 2 in the 90° specimen is due to its size in comparison with the intervoid ligament, which makes it more sensitive to small changes in the surrounding microstructure when different classifier models are used.

Given these results, the re-utilization of a properly trained classifier model for different specimens of the same nature seems feasible. However, care must be exercised when dealing with sensitive variables or with very local information close to the boundaries of the segmented phases.

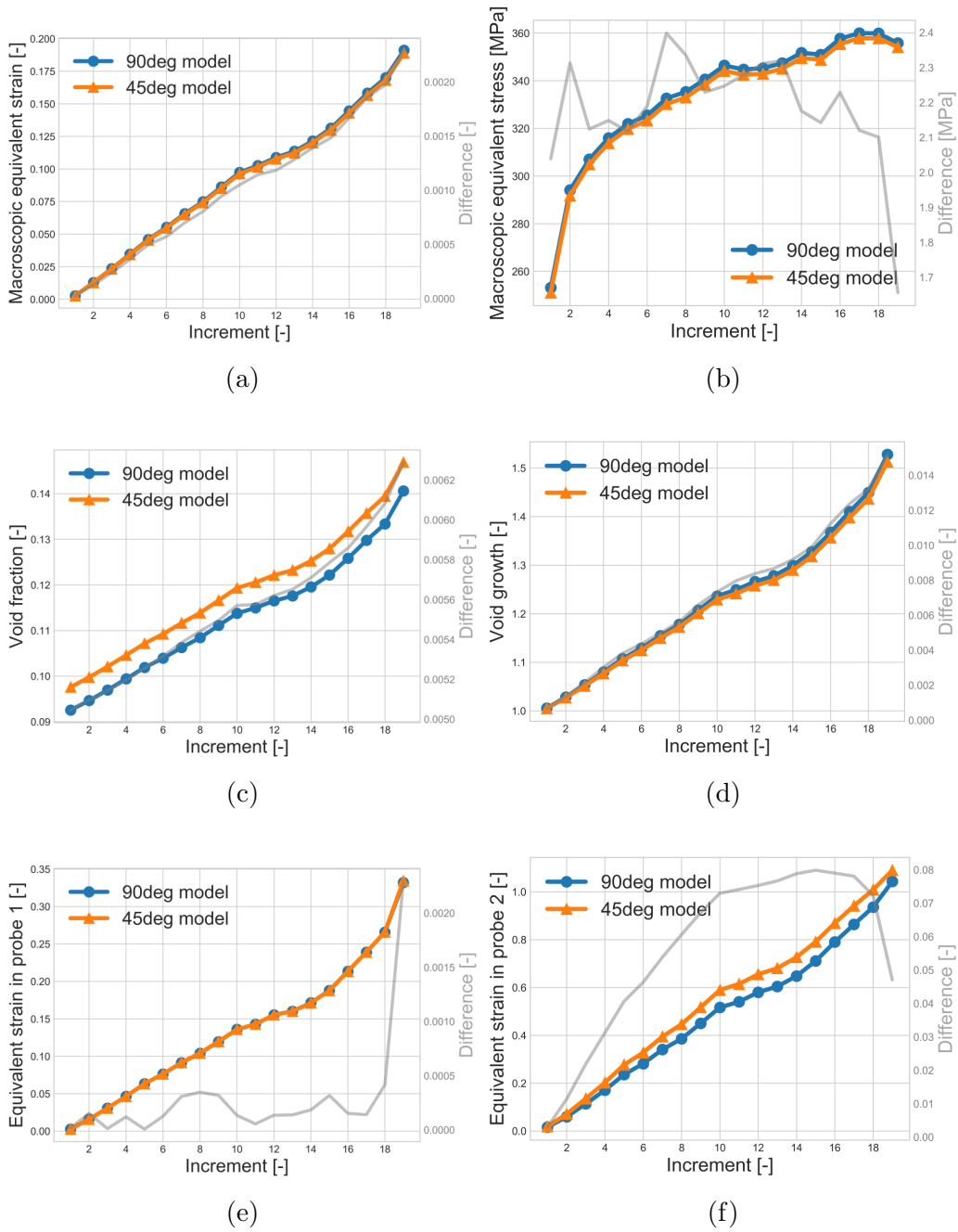


Figure 17: (a) Macroscopic equivalent strain and (b) stress, (c) void volume fraction, (d) void growth, and equivalent strain in (e) probe 1 (f) probe 2 for the 90° simulation obtained after segmentation with two different classifier models.

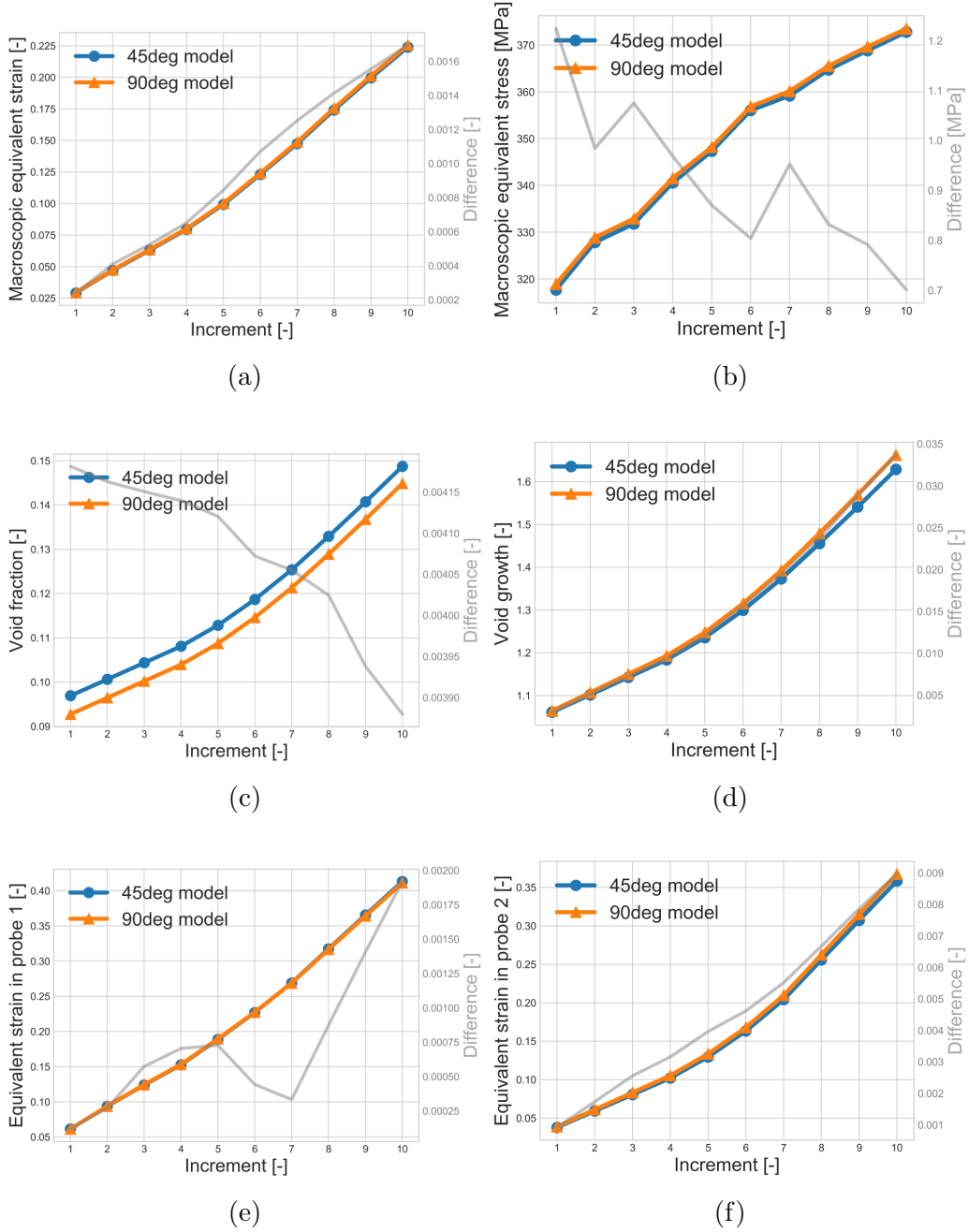


Figure 18: (a) Macroscopic equivalent strain and (b) stress, (c) void volume fraction, (d) void growth, and equivalent strain in (e) probe 1 (f) probe 2 for the 45° simulation obtained after segmentation with two different classifier models.

3.3 Comparison of segmentation methods

Numerical simulations were carried out after immersing the segmented images of the microstructures obtained by means of the segmentation procedures. The results of the numerical simulations are compared to assess the effect of the segmentation procedures on the observables described in Section 2.4.

First, a qualitative comparison of the images segmented with the three different methods is reported in Figure 19 alongside the original slice. The chosen slice is the mid-thickness of the 90° specimen. The three segmented images are similar, albeit with some differences. The image segmented through simple thresholding includes very small voids and some apparent noise. The resulting segmented images from the IsoData and Random forest algorithms are smoothed out in terms of lost features. However, secondary effects are related to filtering out the finest microstructural features and slightly smoothing the interfaces.

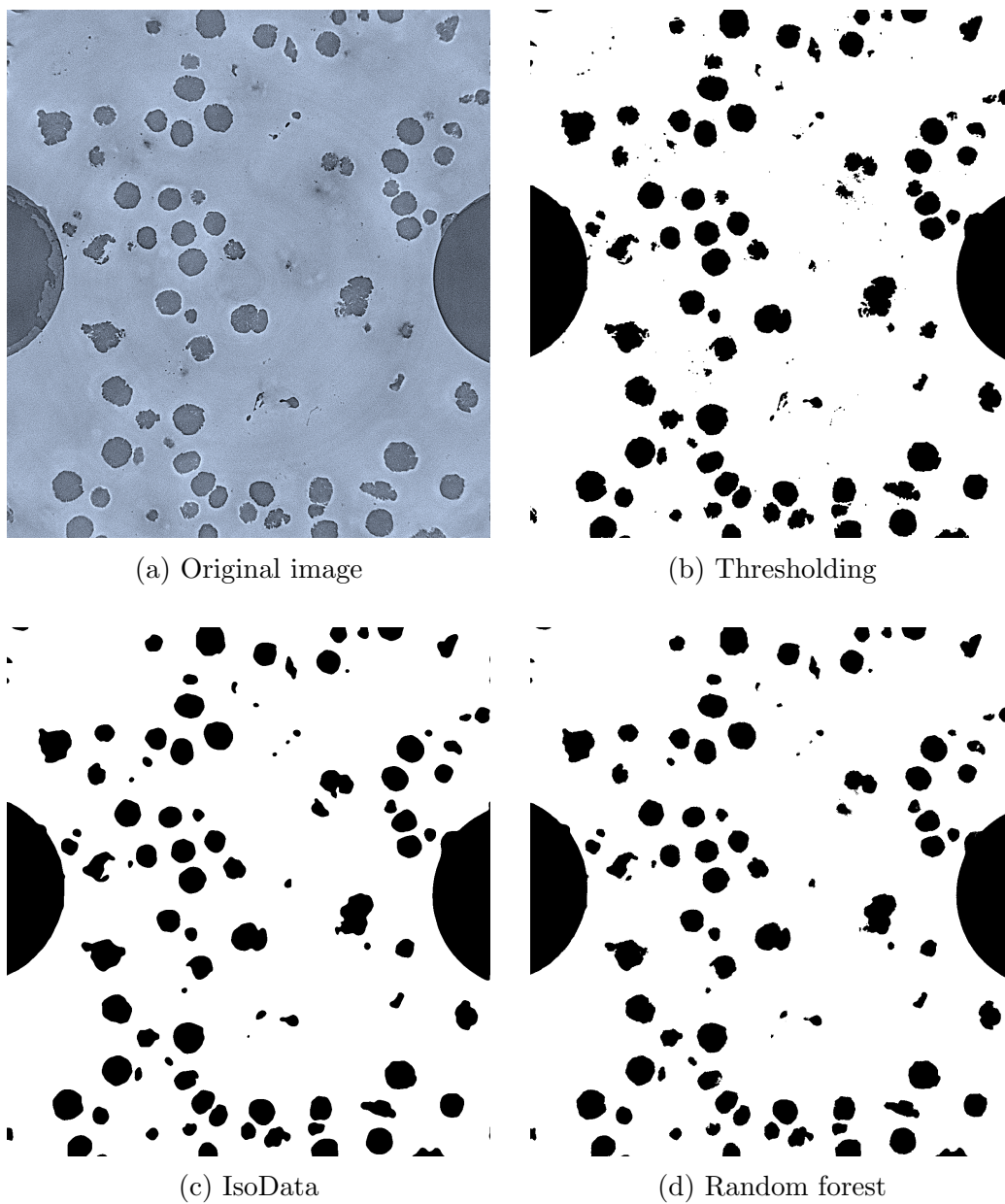


Figure 19: Original mid-thickness slice of the 90° specimen, and the same slice segmented with three different procedures.

From a quantitative point of view, gray level differences can be computed between the original image f and its thresholded (and binarized) copy f_{th} after accounting for global gray level corrections. In the following, linear

corrections are considered

$$g_{th} = a f_{th} + b \quad (5)$$

where a and b are obtained by least squares minimization of the sum of squared gray level differences over the region of interest (ROI) so that

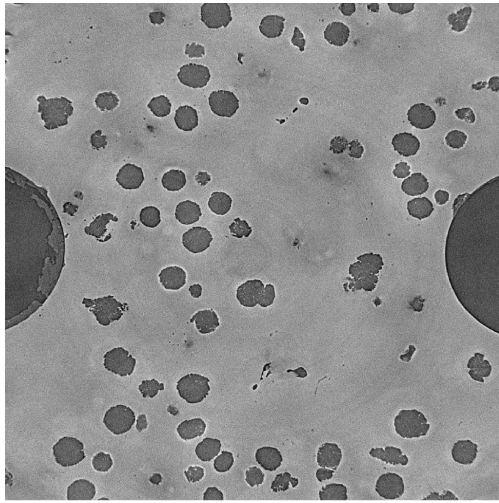
$$r(\mathbf{x}) = f(\mathbf{x}) - g_{th}(\mathbf{x}) \quad (6)$$

will measure the gray level residuals that are computed for any voxel location \mathbf{x} in the ROI. In Table 3, the three different methods are compared for both specimens in terms of their root mean square residuals r_{RMS} . The RMS values are very similar for the three procedures and both specimens, *i.e.*, the segmented images are of comparable quality irrespective of the segmentation procedure.

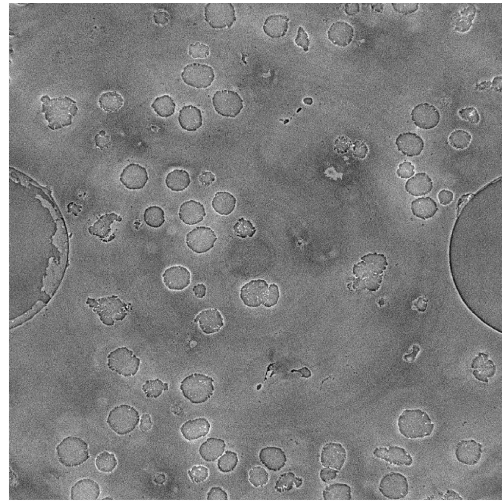
Table 3: Comparison of the gray level residuals for the three thresholding methods for the entire ROI in both specimens.

Procedure	a	b	RMS(r)	Specimen
Thresholding	-0.256	151.7	22.3	90°
IsoData	-0.243	151.1	23.5	90°
Random forest	-0.241	150.5	24.1	90°
Thresholding	-0.261	151.7	22.0	45°
IsoData	-0.249	150.9	23.3	45°
Random forest	-0.260	151.3	22.5	45°

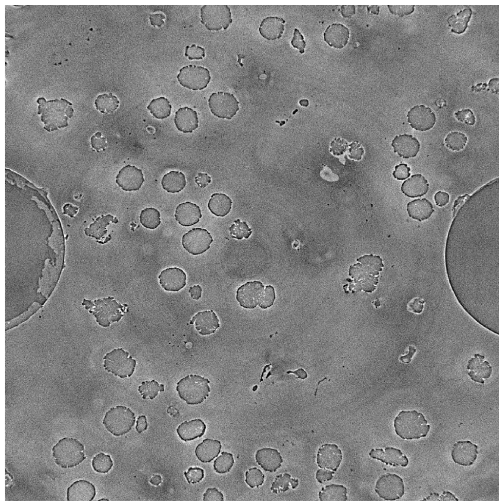
The calculated gray level residuals are shown in Figure 20 for the mid-thickness slice of the 90° specimen. They show a very similar behavior in the bulk of the matrix and present more significant differences close to the interfaces.



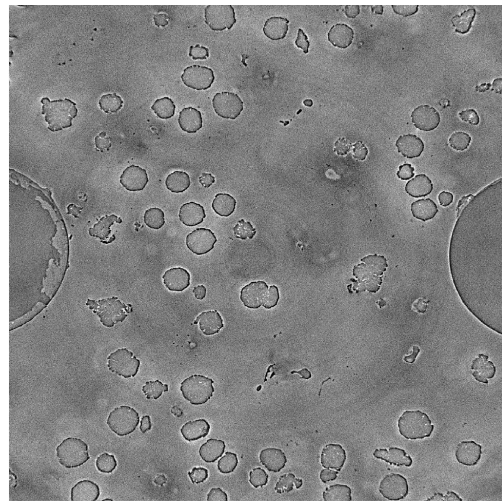
(a) Original image



(b) Thresholding



(c) IsoData



(d) Random forest

Figure 20: (a) Original mid-thickness slice of the 90° specimen, and the corresponding gray level residuals for the segmented image with (b) thresholding, (c) IsoData and (d) random forest algorithms.

For the FE simulations, neither the amount of noise left by the thresholding procedure, nor the loss of the smallest microstructural features with the other two procedures are problematic. The minimum allowed FE mesh size, which was based on the resolution of the images (Section 3.1), does not

capture the remaining noise or the smallest features. The differences that can be perceived by the FE mesh are the non-negligible void shape variations and difference in void volume fraction due to how each method handles partial-volume effects, *i.e.*, how the position of the interfaces is determined.

The results for the six observables with the three segmentation procedures are shown in Figure 21 for the 90° specimen and in Figure 22 for the 45° specimen. The maximum absolute difference is also reported in the figures for all the observables, and it is calculated as the maximum difference between the three results.

In the simulation of the 45° specimen, the macroscopic equivalent strain and stress (Figure 22) exhibit a very small absolute difference. The maximum difference for the macroscopic equivalent strain is 0.0025, and 1.1 MPa for the macroscopic equivalent stress. For the 90° specimen (Figure 21), these variables are slightly higher, but sufficiently small, namely 0.005 and 5.2 MPa for the macroscopic equivalent strain and stress, respectively.

The void growth presents a maximum absolute difference of 0.015 for the 45° specimen (Figure 22d), and 0.03 for the 90° specimen (Figure 21d). The void volume fraction exhibits higher absolute difference than the void growth for both specimens. In the 45° simulation (Figure 22c), the void volume fraction has a maximum absolute difference of 0.005, and 0.014 in the 90° simulation (Figure 21d). In the former specimen, the IsoData and Random forest algorithms coincide remarkably, while for the latter specimen, both thresholding methods produce similar results and the void volume fraction predicted with the random forest algorithm is farther away.

The results in the local probes are more sensitive than the macroscopic observables. For both specimens (Figure 21e for the 90° specimen, and Figure 22e for the 45° specimen), the equivalent strain in probe 1 has a lower maximum absolute difference (*i.e.*, 0.013 for the 90° specimen, and 0.007 for the 45° sample) than the equivalent strain in probe 2 (0.085 for the 90° specimen, and 0.014 for the 45° sample). The absolute difference for probe 2 in the

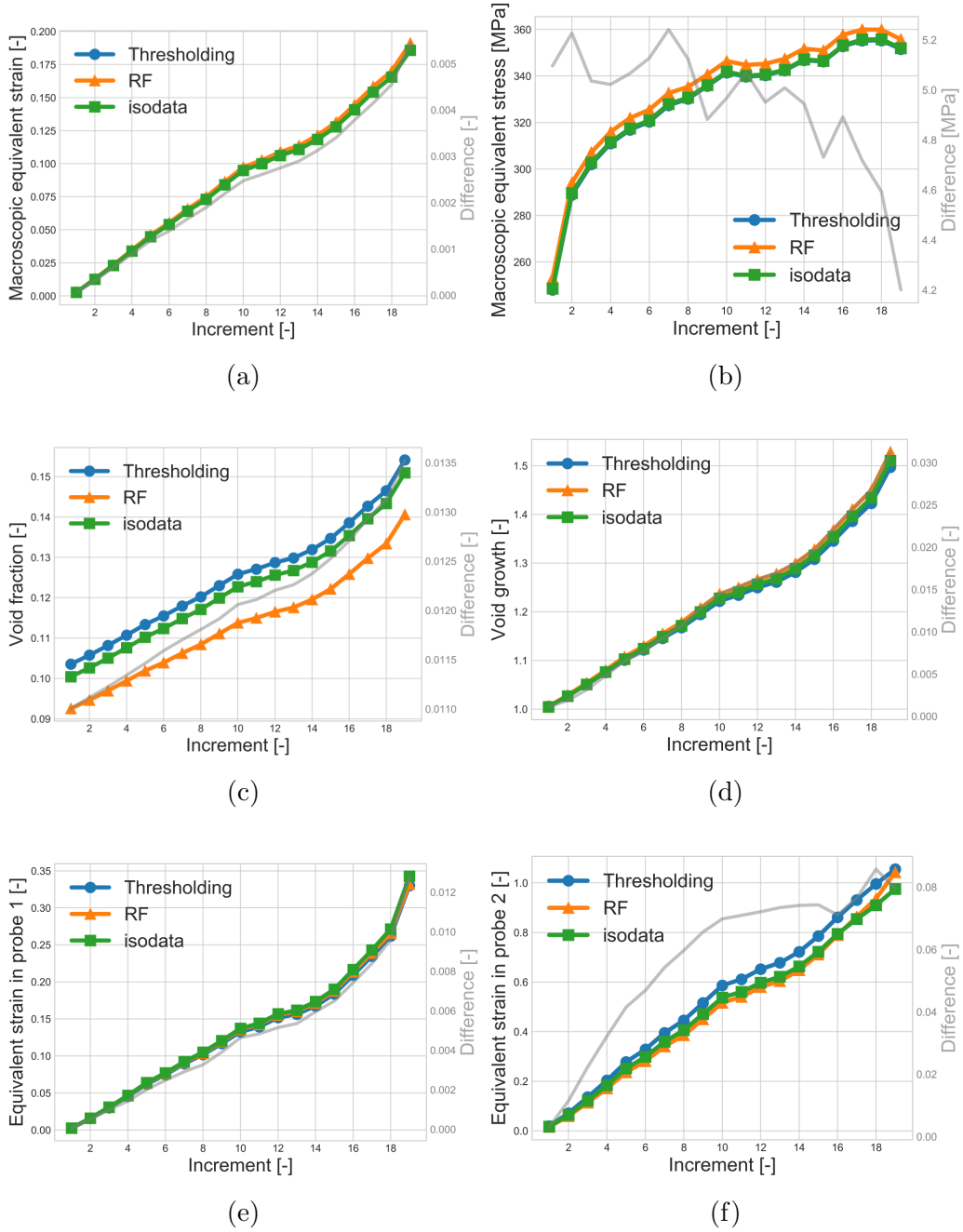


Figure 21: (a) Macroscopic equivalent strain and (b) stress, (c) void volume fraction, (d) void growth, and equivalent strain in (e) probe 1 (f) probe 2 for the 90° simulation obtained after segmentation with three different segmentation procedures.

90° simulation is notably high. Since probe 2 of the 90° specimen is smaller and located in a shorter intervoid ligament, it is more sensitive to changes in its neighborhood due to the use of different segmentation procedures. In general, the proximity of a probe to void interfaces is correlated with higher levels of absolute differences. The DVC standard equivalent strain resolutions were estimated to be 0.78% for the 90° configuration and 0.73% for the 45° [25]. The segmentation-related uncertainty is at best equivalent (probe 1 of the 45° specimen) to the DVC uncertainties, but between 2 and 10 times higher for the other observables.

The comparisons carried out herein show that the results of the FE simulations with immersed images stemming from the employed segmentation methods, are sufficiently small so that physical conclusions may be drawn from the results of the simulations and the segmentation procedures are hence considered to be successful. The most sensitive variables to the choice of segmentation method could be identified, namely, the local strain values and the void volume fraction.

In terms of user input, automatic thresholding with the IsoData algorithm is the least demanding methodology since it requires no user intervention. It is followed by simple thresholding by inspection for which the threshold is set from the gray level histogram. The Random forest procedure needs user input for the training of the model, and possibly the choice of parameters and filters if their default values are unsatisfactory. The need for user input may hinder the application of a methodology in an automatic procedure starting at the image acquisition and continuing all the way up to the postprocessing of the FE simulations. However, the last two methodologies may also be incorporated into a fully automated procedure given that the step that requires some user input can be carried out once and applied to several cases of similar features.

The manual and automatic thresholding procedures may easily be carried out with limited computing resources. The random forest procedure does re-

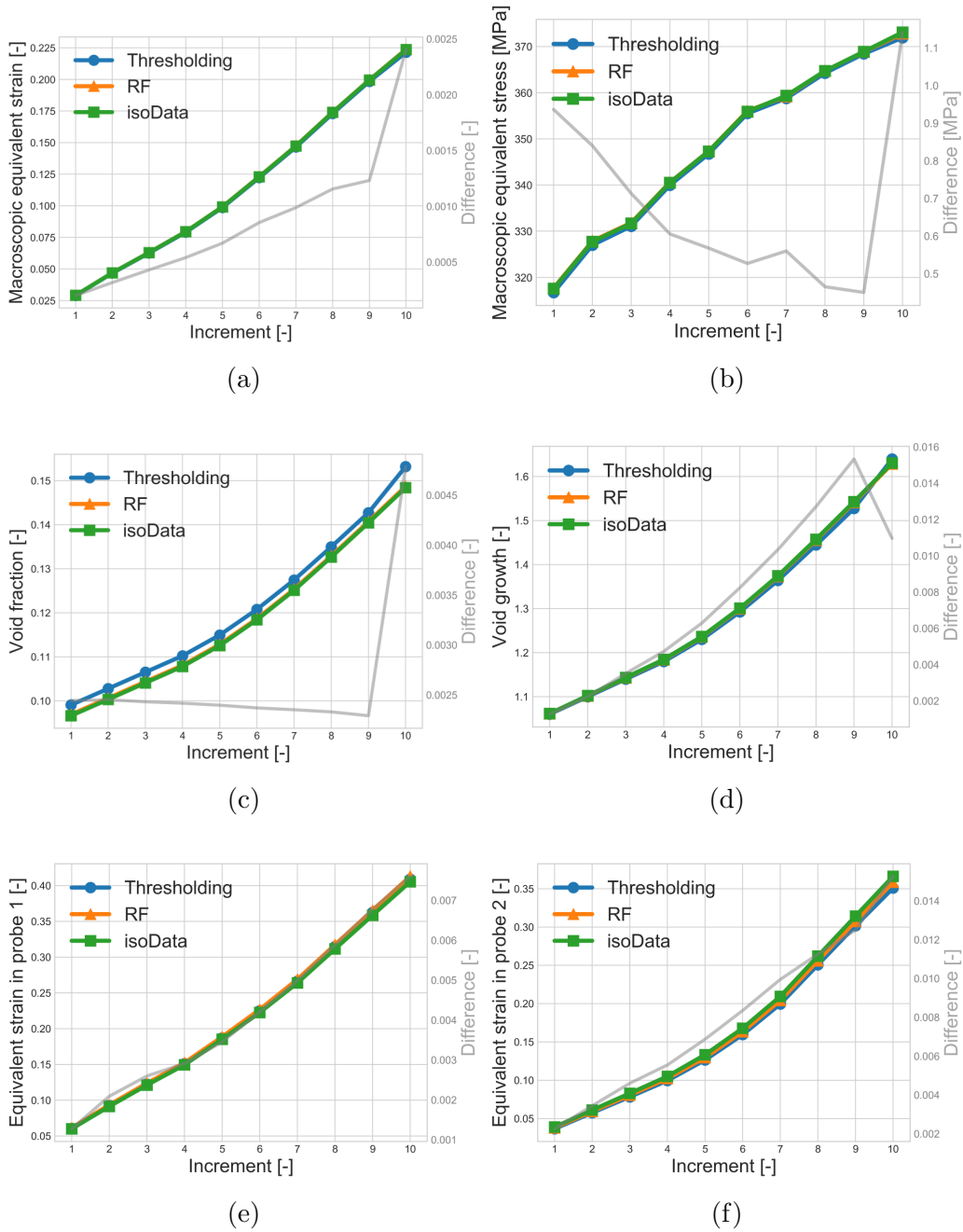


Figure 22: (a) Macroscopic equivalent strain and (b) stress, (c) void volume fraction, (d) void growth, and equivalent strain in (e) probe 1 (f) probe 2 for the 45° simulation obtained after segmentation with three different segmentation procedures.

quire more significant resources in terms of memory and computing time. For this reason, it may be reserved for more complex cases in which thresholding is not viable if the needed computational capacity is not available. More generally, even in cases when thresholding is feasible, it may still be desirable to use the random forest algorithm to provide means for cross-verification.

3.4 Uncertainty quantification

The comparison of segmentation procedures discussed in Section 3.3 is summarized via uncertainty estimations. Three different predictions resulting from the three considered segmentation procedures are available for each observable. To estimate its uncertainty, the average and standard deviation are calculated. This is conducted separately for each of the observables. The calculated averages and standard deviations are not statistically representative quantities because they are calculated based on only three data sets. They are used here as a concise way of presenting a single measurement and its associated uncertainty. This will be useful in future works when these data will be compared with experimental measurements. The uncertainty estimation was carried out for all of the observables and both samples. The results described in Section 3.3 showed that global volume-averaged strain and stress, as well as void growth, are not very sensitive to the choice of the segmentation procedures employed in this work. For the sake of brevity, the uncertainty for the most sensitive variables is discussed in this section.

Figure 23 shows the change of the average void volume fraction for both specimen, and Figure 24, that of the average equivalent strain for the two probes of the 90° simulations. In both figures, the corresponding standard deviation is presented as error bars.

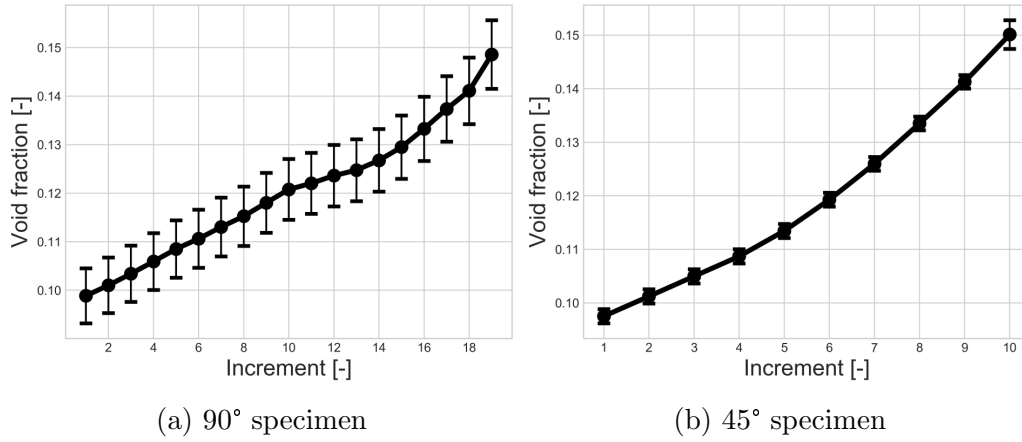


Figure 23: Average of the results of the three segmentation procedures for the void volume fraction with its estimated uncertainty (error bars) in (a) the 90° simulation, and (b) the 45° simulation.

The difference of uncertainties reported for the void volume fraction between the two specimens in Figure 23 is noteworthy. This difference exists even though the same segmentation methodologies were applied. Ambiguous determination of the position of interfaces due to partial-volume effects and human factors during data treatment are at the origin of this difference. This observation highlights the importance of dedicating sufficient effort to the image segmentation step and uncertainty estimation when feasible. A disregard of present uncertainties may lead to biased physical conclusions.

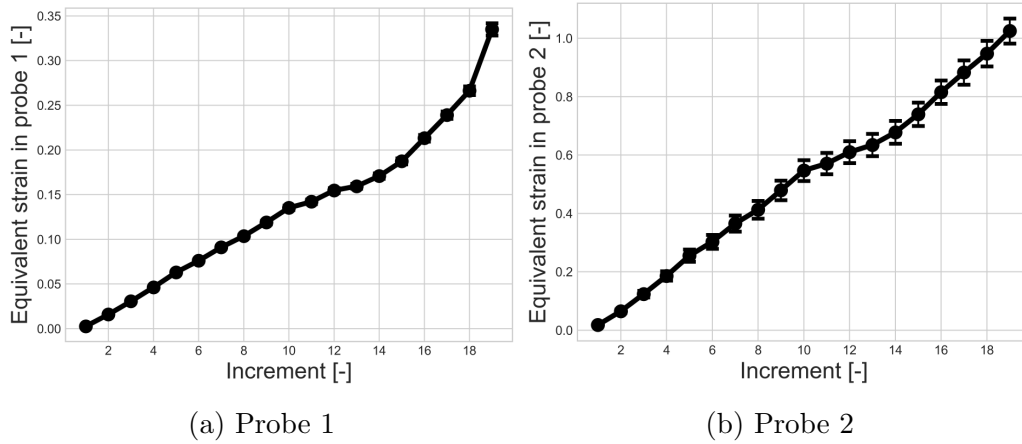


Figure 24: Average and standard deviation (error bars) of the results of the three segmentation procedures in the 90° simulation for the equivalent strain (a) in probe 1 and (b) probe 2.

Since probe 2 is located in a small intervoid ligament, i.e., closer to the void-matrix interface, it presents larger uncertainties than probe 1. For both probes the uncertainty, depicted in Figure 24, increases during the simulation, but remains satisfactorily small.

4 Conclusions and perspectives

A comparative study of three segmentation procedures dedicated to the so-called SRCL-DVC-FE methodology was carried out in the context of micromechanical studies of ductile damage. The focus of the conducted analysis was on the effect of image segmentation techniques on the results of FE simulations. To the best of the authors' knowledge, this is the first work to document and quantify the effect of image segmentation on the mechanical results of simulations of immersed microstructures. This is relevant for all simulations with immersed microstructures and not only for the SRCL-DVC-FE framework.

Different segmentation procedures were considered, and three were selected and presented in detail. They satisfactorily segmented the three-dimensional images. Six different observables were taken into account for each of the two studied nodular graphite cast iron samples (*i.e.*, macroscopic equivalent strain and stress, void volume fraction and growth, and local equivalent strain in two probes in different intervoid ligaments).

The three segmentation procedures were compared in terms of the resulting gray level residuals, of the required computing power and of the required user input. The gray level residuals were very similar for the different procedures. For this reason, the choice of preferred segmentation method depends on the complexity of the problem, the available computing power and the acceptable level of user input. Multiple methods should be employed and compared whenever possible.

First, a mesh sensitivity analysis was conducted to check that the influence of the spatial discretization on the observables was sufficiently small. Care was taken not to use mesh sizes smaller than the order of magnitude of the laminography images resolution. The most sensitive parameters were identified, namely, the local strain values and the void volume fraction, and sufficiently small mesh dependence was reached.

Second, the segmented images were then immersed in an FE mesh and micromechanical calculations with realistic boundary conditions were carried out. The results were compared in terms of the six different observables. A small sensitivity for the macroscopic behavior was found. A maximum relative difference less than 3% was obtained for the macroscopic strain and stress. It is believed that this overall agreement is mainly due to the fact that the (same) measured boundary conditions were prescribed. The void volume fraction and the local strains were the most sensitive variables. The void volume fraction was considerably more sensitive for the 90° specimen (maximum absolute difference of 0.014) than for the 45° specimen (maximum absolute difference of 0.005). The maximum absolute difference in the local

strain measures varied from 0.007 to 0.085 and increased with the proximity of the probed volume to the void-matrix interface.

The differences in uncertainty for the void volume fraction across specimens resulted from applying the same segmentation procedures in the same material by the same operator. This highlights the challenges associated with the use of immersed images in FE simulations. They originate from two factors, namely, the ambiguity in the position of the segmented interfaces due to partial-volume effects, and the possible bias introduced by the operator.

An uncertainty quantification based on the comparison of segmentation methods was proposed. Since FE simulations were based on three different segmentation procedures, the uncertainty of an observable was estimated as the standard deviation of the results of the three FE simulations and reported alongside the corresponding average. The estimated uncertainty will be used in future works to compare in detail numerical results with experimental observations for validation purposes.

Data availability statement

The raw/processed data required to reproduce these findings cannot be shared at this time as the data also forms part of an ongoing study.

Acknowledgements

This work was performed within the COMINSIDE project funded by the French Agence Nationale de la Recherche (ANR-14-CE07-0034-02 grant).

References

- [1] S. Youssef, E. Maire, and R. Gaertner, “Finite element modelling of the actual structure of cellular materials determined by x-ray tomography,” *Acta Materialia*, vol. 53, no. 3, pp. 719–730, 2005.
- [2] N. Vanderesse, E. Maire, A. Chabod, and J.-Y. Buffière, “Microtomographic study and finite element analysis of the porosity harmfulness in a cast aluminium alloy,” *International Journal of Fatigue*, vol. 33, no. 12, pp. 1514–1525, 2011.
- [3] A. Buljac, M. Shakoor, J. Neggers, M. Bernacki, P.-O. Bouchard, L. Helfen, T. F. Morgeneyer, and F. Hild, “Numerical validation framework for micromechanical simulations based on synchrotron 3D imaging,” *Computational Mechanics*, vol. 59, no. 3, pp. 419–441, 2017.
- [4] M. Shakoor, A. Buljac, J. Neggers, F. Hild, T. F. Morgeneyer, L. Helfen, M. Bernacki, and P.-O. Bouchard, “On the choice of boundary conditions for micromechanical simulations based on 3D imaging,” *International Journal of Solids and Structures*, vol. 112, pp. 83–96, 2017.
- [5] A. Buljac, V. M. Trejo Navas Navas, M. Shakoor, A. Bouterf, J. Neggers, M. Bernacki, P.-O. Bouchard, T. F. Morgeneyer, and F. Hild, “On the calibration of elastoplastic parameters at the microscale via x-ray microtomography and digital volume correlation for the simulation of ductile damage,” *European Journal of Mechanics-A/Solids*, vol. 72, p. 287.
- [6] D. L. Pham, C. Xu, and J. L. Prince, “Current methods in medical image segmentation,” *Annual review of biomedical engineering*, vol. 2, no. 1, pp. 315–337, 2000.
- [7] P. Iassonov, T. Gebrenegus, and M. Tuller, “Segmentation of x-ray computed tomography images of porous materials: A crucial step for characterization and quantitative analysis of pore structures,” *Water Resources Research*, vol. 45, no. 9, 2009.

- [8] M. Sezgin and B. Sankur, “Survey over image thresholding techniques and quantitative performance evaluation,” *Journal of Electronic imaging*, vol. 13, no. 1, pp. 146–166, 2004.
- [9] L. Staniewicz and P. A. Midgley, “Machine learning as a tool for classifying electron tomographic reconstructions,” *Advanced Structural and Chemical Imaging*, vol. 1, no. 1, p. 9, 2015.
- [10] L.-C. Chen, G. Papandreou, I. Kokkinos, K. Murphy, and A. L. Yuille, “Deeplab: Semantic image segmentation with deep convolutional nets, atrous convolution, and fully connected crfs,” *arXiv preprint arXiv:1606.00915*, 2016.
- [11] A. Madra, N. El Hajj, and M. Benzeggagh, “X-ray microtomography applications for quantitative and qualitative analysis of porosity in woven glass fiber reinforced thermoplastic,” *Composites Science and Technology*, vol. 95, pp. 50–58, 2014.
- [12] D. S. Bulgarevich, S. Tsukamoto, T. Kasuya, M. Demura, and M. Watanabe, “Pattern recognition with machine learning on optical microscopy images of typical metallurgical microstructures,” *Scientific reports*, vol. 8, no. 1, p. 2078, 2018.
- [13] L. Helfen, T. Baumbach, P. Mikulik, D. Kiel, P. Pernot, P. Cloetens, and J. Baruchel, “High-resolution three-dimensional imaging of flat objects by synchrotron-radiation computed laminography,” *Applied Physics Letters*, vol. 86, no. 7, p. 071915, 2005.
- [14] T. F. Morgeneyer, L. Helfen, H. Mubarak, and F. Hild, “3d digital volume correlation of synchrotron radiation laminography images of ductile crack initiation: an initial feasibility study,” *Experimental Mechanics*, vol. 53, no. 4, pp. 543–556, 2013.
- [15] M. Shakoar, P.-O. Bouchard, and M. Bernacki, “An adaptive level-set method with enhanced volume conservation for simulations in multi-phase domains,” *International Journal for Numerical Methods in Engineering*, vol. 109, no. 4, pp. 555–576, 2017.

- [16] A. Buljac, T. Taillandier-Thomas, L. Helfen, T. F. Morgeneyer, and F. Hild, “Evaluation of measurement uncertainties of digital volume correlation applied to laminography data,” *The Journal of Strain Analysis for Engineering Design*, vol. 53, pp. 49–65, 2018.
- [17] C. Labrecque and M. Gagne, “Ductile iron: fifty years of continuous development,” *Canadian Metallurgical Quarterly*, vol. 37, no. 5, pp. 343–378, 1998.
- [18] M. Kuna, M. Springmann, K. Mädler, P. Hübner, and G. Pusch, “Fracture mechanics based design of a railway wheel made of austempered ductile iron,” *Engineering Fracture Mechanics*, vol. 72, no. 2, pp. 241–253, 2005.
- [19] M. Shirani and G. Härkegård, “Fatigue life distribution and size effect in ductile cast iron for wind turbine components,” *Engineering Failure Analysis*, vol. 18, no. 1, pp. 12–24, 2011.
- [20] G. Huetter, L. Zybell, and M. Kuna, “Micromechanisms of fracture in nodular cast iron: From experimental findings towards modeling strategies—a review,” *Engineering Fracture Mechanics*, vol. 144, pp. 118–141, 2015.
- [21] V. Tvergaard and A. Needleman, “Three dimensional microstructural effects on plane strain ductile crack growth,” *International journal of solids and structures*, vol. 43, no. 20, pp. 6165–6179, 2006.
- [22] G. Hütter, L. Zybell, and M. Kuna, “Micromechanical modeling of crack propagation in nodular cast iron with competing ductile and cleavage failure,” *Engineering Fracture Mechanics*, vol. 147, pp. 388–397, 2015.
- [23] L. Helfen, A. Myagotin, A. Rack, P. Pernot, P. Mikulik, M. Di Michiel, and T. Baumbach, “Synchrotron-radiation computed laminography for high-resolution three-dimensional imaging of flat devices,” *physica status solidi (a)*, vol. 204, no. 8, pp. 2760–2765, 2007.

- [24] A. Buljac, C. Jailin, A. Mendoza, J. Neggers, T. Taillandier-Thomas, A. Bouterf, B. Smaniotto, F. Hild, and S. Roux, “Digital volume correlation: Review of progress and challenges,” *Experimental Mechanics*, vol. 58, no. 5, pp. 661–708, 2018.
- [25] A. Buljac, L. Helfen, F. Hild, and T. F. Morgeneyer, “Effect of void arrangement on ductile damage mechanisms in nodular graphite cast iron: In situ 3d measurements,” *Engineering Fracture Mechanics*, vol. 192, pp. 242–261, 2018.
- [26] Z. Tomičević, J. Kodvanj, and F. Hild, “Characterization of the non-linear behavior of nodular graphite cast iron via inverse identification. Analysis of uniaxial tests,” *Europ. J. Mech. A/Solids*, vol. 59, pp. 140–154, 2016.
- [27] J. Schindelin, I. Arganda-Carreras, E. Frise, V. Kaynig, M. Longair, T. Pietzsch, S. Preibisch, C. Rueden, S. Saalfeld, B. Schmid, *et al.*, “Fiji: an open-source platform for biological-image analysis,” *Nature methods*, vol. 9, no. 7, p. 676, 2012.
- [28] C. A. Schneider, W. S. Rasband, and K. W. Eliceiri, “Nih image to imagej: 25 years of image analysis,” *Nature methods*, vol. 9, no. 7, p. 671, 2012.
- [29] R. Adams and L. Bischof, “Seeded region growing,” *IEEE Transactions on pattern analysis and machine intelligence*, vol. 16, no. 6, pp. 641–647, 1994.
- [30] J. A. Sethian, *Level set methods and fast marching methods: evolving interfaces in computational geometry, fluid mechanics, computer vision, and materials science*, vol. 3. Cambridge university press, 1999.
- [31] T. Ridler, S. Calvard, *et al.*, “Picture thresholding using an iterative selection method,” *IEEE trans syst Man Cybern*, vol. 8, no. 8, pp. 630–632, 1978.

- [32] L.-K. Huang and M.-J. J. Wang, “Image thresholding by minimizing the measures of fuzziness,” *Pattern recognition*, vol. 28, no. 1, pp. 41–51, 1995.
- [33] J. Prewitt and M. L. Mendelsohn, “The analysis of cell images,” *Annals of the New York Academy of Sciences*, vol. 128, no. 1, pp. 1035–1053, 1966.
- [34] C. Li and P. K.-S. Tam, “An iterative algorithm for minimum cross entropy thresholding,” *Pattern recognition letters*, vol. 19, no. 8, pp. 771–776, 1998.
- [35] C. H. Li and C. Lee, “Minimum cross entropy thresholding,” *Pattern recognition*, vol. 26, no. 4, pp. 617–625, 1993.
- [36] J. N. Kapur, P. K. Sahoo, and A. K. Wong, “A new method for gray-level picture thresholding using the entropy of the histogram,” *Computer vision, graphics, and image processing*, vol. 29, no. 3, pp. 273–285, 1985.
- [37] C. A. Glasbey, “An analysis of histogram-based thresholding algorithms,” *CVGIP: Graphical models and image processing*, vol. 55, no. 6, pp. 532–537, 1993.
- [38] J. Kittler and J. Illingworth, “Minimum error thresholding,” *Pattern recognition*, vol. 19, no. 1, pp. 41–47, 1986.
- [39] W.-H. Tsai, “Moment-preserving thresholding: A new approach,” *Computer Vision, Graphics, and Image Processing*, vol. 29, no. 3, pp. 377–393, 1985.
- [40] N. Otsu, “A threshold selection method from gray-level histograms,” *IEEE transactions on systems, man, and cybernetics*, vol. 9, no. 1, pp. 62–66, 1979.
- [41] W. Doyle, “Operations useful for similarity-invariant pattern recognition,” *Journal of the ACM (JACM)*, vol. 9, no. 2, pp. 259–267, 1962.

- [42] A. Rényi, “On measures of entropy and information,” tech. rep., HUNGARIAN ACADEMY OF SCIENCES Budapest Hungary, 1961.
- [43] A. G. Shanbhag, “Utilization of information measure as a means of image thresholding,” *CVGIP: Graphical Models and Image Processing*, vol. 56, no. 5, pp. 414–419, 1994.
- [44] G. Zack, W. Rogers, and S. Latt, “Automatic measurement of sister chromatid exchange frequency,” *Journal of Histochemistry & Cytochemistry*, vol. 25, no. 7, pp. 741–753, 1977.
- [45] J.-C. Yen, F.-J. Chang, and S. Chang, “A new criterion for automatic multilevel thresholding,” *IEEE Transactions on Image Processing*, vol. 4, no. 3, pp. 370–378, 1995.
- [46] L. Breiman, “Random forests,” *Machine learning*, vol. 45, no. 1, pp. 5–32, 2001.
- [47] I. Arganda-Carreras, V. Kaynig, C. Rueden, K. W. Eliceiri, J. Schindelin, A. Cardona, and H. Sebastian Seung, “Trainable weka segmentation: a machine learning tool for microscopy pixel classification,” *Bioinformatics*, vol. 33, no. 15, pp. 2424–2426, 2017.
- [48] D.-L. Quan, T. Toulorge, E. Marchandise, J.-F. Remacle, and G. Briceux, “Anisotropic mesh adaptation with optimal convergence for finite elements using embedded geometries,” *Computer Methods in Applied Mechanics and Engineering*, vol. 268, pp. 65–81, 2014.
- [49] M. Shakoor, M. Bernacki, and P.-O. Bouchard, “Ductile fracture of a metal matrix composite studied using 3d numerical modeling of void nucleation and coalescence,” *Engineering Fracture Mechanics*, vol. 189, pp. 110–132, 2017.
- [50] H. Digonnet, L. Silva, and T. Coupez, “Cimlib: a fully parallel application for numerical simulations based on components assembly,” in *AIP Conference Proceedings*, vol. 908, pp. 269–274, AIP, 2007.

- [51] F. Brezzi, D. Boffi, L. Demkowicz, R. Durán, R. Falk, and M. Fortin, *Mixed finite elements, compatibility conditions, and applications*. Springer, 2008.
- [52] M. Shakoov, M. Bernacki, and P.-O. Bouchard, “A new body-fitted immersed volume method for the modeling of ductile fracture at the microscale: Analysis of void clusters and stress state effects on coalescence,” *Engineering Fracture Mechanics*, vol. 147, pp. 398–417, 2015.
- [53] E. Roux, M. Bernacki, and P.-O. Bouchard, “A level-set and anisotropic adaptive remeshing strategy for the modeling of void growth under large plastic strain,” *Computational Materials Science*, vol. 68, pp. 32–46, 2013.